

REANALYSIS OF DATA TAKEN BY THE CANGAROO 3.8 METER IMAGING ATMOSPHERIC CHERENKOV  
TELESCOPE: PSR B1706–44, SN 1006, AND VELAT. YOSHIKOSHI<sup>1</sup>, M. MORI<sup>1,2</sup>, P. G. EDWARDS<sup>3</sup>, S. GUNJI<sup>4</sup>, S. HARA<sup>5</sup>, T. HARA<sup>6</sup>, A. KAWACHI<sup>7</sup>, Y. MIZUMOTO<sup>8</sup>,  
T. NAITO<sup>6</sup>, K. NISHIJIMA<sup>7</sup>, T. TANIMORI<sup>9</sup>, G. J. THORNTON<sup>10</sup>, AND T. YOSHIDA<sup>11</sup>*Draft version August 19, 2009*

## ABSTRACT

We have reanalyzed data from observations of PSR B1706–44, SN 1006, and the Vela pulsar region made with the CANGAROO 3.8m Imaging Atmospheric Cherenkov Telescope between 1993 and 1998 in response to the results reported for these sources by the H.E.S.S. Collaboration. Although detections of TeV gamma-ray emission from these sources were claimed by CANGAROO more than 10 years ago, upper limits to the TeV gamma-ray signals from PSR B1706–44 and SN 1006 derived by H.E.S.S. are about an order of magnitude lower. The H.E.S.S. group detected strong diffuse TeV gamma-ray emission from Vela but with a morphology differing from the CANGAROO result. In our reanalysis, in which gamma-ray selection criteria have been determined exclusively using gamma-ray simulations and OFF-source data as background samples, no significant TeV gamma-ray signals have been detected from compact regions around PSR B1706–44 or within the northeast rim of SN 1006. The upper limits to the integral gamma-ray fluxes at the 95% confidence level have been estimated for the 1993 data of PSR B1706–44 to be  $F(> 3.2 \pm 1.6 \text{ TeV}) < 8.03 \times 10^{-13} \text{ photons cm}^{-2} \text{ s}^{-1}$ , for the 1996 and 1997 data of SN 1006 to be  $F(> 3.0 \pm 1.5 \text{ TeV}) < 1.20 \times 10^{-12} \text{ photons cm}^{-2} \text{ s}^{-1}$  and  $F(> 1.8 \pm 0.9 \text{ TeV}) < 1.96 \times 10^{-12} \text{ photons cm}^{-2} \text{ s}^{-1}$ , respectively. We discuss reasons why the original analyses gave the source detections. The reanalysis did result in a TeV gamma-ray signal from the Vela pulsar region at the  $4.5\sigma$  level using 1993, 1994, and 1995 data. The excess was located at the same position,  $0^\circ 13'$  to the southeast of the Vela pulsar, as that reported in the original analysis. We have investigated the effect of the acceptance distribution in the field of view of the 3.8m telescope, which rapidly decreases toward the edge of the field of the camera, on the detected gamma-ray morphology. The expected excess distribution for the 3.8m telescope has been obtained by reweighting the distribution of HESS J0835–455 measured by H.E.S.S. with the acceptance of the 3.8m telescope. The result is morphologically comparable to the CANGAROO excess distribution, although the profile of the acceptance-reweighted H.E.S.S. distribution is more diffuse than that of CANGAROO. The integral gamma-ray flux from HESS J0835–455 has been estimated for the same region as defined by H.E.S.S. from the 1993–1995 data of CANGAROO to be  $F(> 4.0 \pm 1.6 \text{ TeV}) = (3.28 \pm 0.92) \times 10^{-12} \text{ photons cm}^{-2} \text{ s}^{-1}$ , which is statistically consistent with the integral flux obtained by H.E.S.S.

*Subject headings:* gamma rays: observations — methods: data analysis — pulsars: individual (PSR B1706–44, Vela pulsar) — supernova remnants — supernovae: individual (SN 1006)

## 1. INTRODUCTION

Electronic address: tyoshiko@icrr.u-tokyo.ac.jp

<sup>1</sup> Institute for Cosmic Ray Research, University of Tokyo, Kashiwa, Chiba 277-8582, Japan.

<sup>2</sup> Current address: Department of Physics, Ritsumeikan University, Kusatsu, Shiga 525-8577, Japan.

<sup>3</sup> Narrabri Observatory, Australia Telescope National Facility, CSIRO, Narrabri, NSW 2390, Australia.

<sup>4</sup> Department of Physics, Yamagata University, Yamagata, Yamagata 990-8560, Japan.

<sup>5</sup> Ibaraki Prefectural University of Health Sciences, Ami, Ibaraki 300-0394, Japan.

<sup>6</sup> Faculty of Management Information, Yamanashi Gakuin University, Kofu, Yamanashi 400-8575, Japan.

<sup>7</sup> Department of Physics, Tokai University, Hiratsuka, Kanagawa 259-1292, Japan.

<sup>8</sup> National Astronomical Observatory of Japan, Mitaka, Tokyo 181-8588, Japan.

<sup>9</sup> Department of Physics, Kyoto University, Sakyo-ku, Kyoto 606-8502, Japan.

<sup>10</sup> School of Chemistry and Physics, University of Adelaide, SA 5005, Australia.

<sup>11</sup> Faculty of Science, Ibaraki University, Mito, Ibaraki 310-8512, Japan.

The CANGAROO<sup>12</sup> 3.8m telescope was an Imaging Atmospheric Cherenkov Telescope (IACT) for TeV gamma-ray astrophysics which operated from 1992 to 1998 near Woomera, South Australia. It is retrospectively called the CANGAROO-I telescope since its pioneering role as the first IACT in the southern hemisphere was subsequently inherited by the CANGAROO-II telescope (Tanimori et al. 1999) and the CANGAROO-III telescope system (Kubo et al. 2004). The discoveries of TeV gamma-ray signals from five sources have been claimed from CANGAROO-I data: PSR B1706–44 (Kifune et al. 1995), the Vela pulsar region (Yoshikoshi et al. 1997), SN 1006 (Tanimori et al. 1998), RX J1713.7–3946 (Muraishi et al. 2000), and PSR B1509–58<sup>13</sup> (Sako et al. 2000). However, H.E.S.S. has later reported upper limits to the TeV gamma-ray

<sup>12</sup> Acronym for the “Collaboration of Australia and Nippon (Japan) for a GAMMA Ray Observatory in the Outback”.

<sup>13</sup> A marginal detection compared to the other CANGAROO-I sources.

fluxes from PSR B1706–44 (Aharonian et al. 2005a) and SN 1006 (Aharonian et al. 2005b), which are lower than the CANGAROO-I fluxes by factors of  $\sim 10$ . The results are obviously inconsistent as the reported statistical significances of the CANGAROO-I detections were  $12\sigma$  for PSR B1706–44 and  $7.7\sigma$  for SN 1006, assuming that the flux levels are constant over the 10 year period. More recently, H.E.S.S. has detected a TeV gamma-ray signal from SN 1006 after accumulating more data (Naumann-Godó et al. 2008), but the flux level is well below their previous upper limit.<sup>14</sup> The Durham group also reported a statistically significant ( $5.9\sigma$ ) detection of TeV gamma rays from PSR B1706–44 (Chadwick et al. 1998). Preliminary support of the TeV gamma-ray signals from PSR B1706–44 and SN 1006 were reported from CANGAROO-II observations (Kushida et al. 2001, 2003; Hara et al. 2001).

H.E.S.S. also observed the Vela pulsar region in 2004 and 2005, and detected a strong gamma-ray signal at the 50% Crab level above 1 TeV (Aharonian et al. 2006a). The emission is diffuse over the X-ray (0.9–2.0 keV) jet-like image, which was first detected by *ROSAT* (Markwardt & Ögelman 1995), and extends about  $1^\circ$  from the pulsar toward the south-southwest, reaching the position of the brightest radio emission in the Vela supernova remnant (SNR), Vela X (Weiler & Panagia 1980). The position of the maximum TeV emission in HESS J0835–455 is located in the middle of the jet-like feature, which has been identified by *Chandra* to be ejected in the direction of the equatorial pulsar wind (Helfand et al. 2001; Pavlov et al. 2003). On the other hand, the TeV emission detected by CANGAROO-I was offset from the pulsar by  $0^\circ.13$  to the southeast (Yoshikoshi et al. 1997), corresponding to the possible pulsar birthplace calculated using the proper motion of  $45 \text{ mas yr}^{-1}$  toward a position angle of  $301^\circ$  (Dodson et al. 2003) and the characteristic age of 11 kyr (Manchester et al. 2005). The CANGAROO-I source thus appears to be different from the H.E.S.S. source, as the angular offset between their peaks is  $0^\circ.34$ , although the position of the CANGAROO-I peak does lie within the region of the H.E.S.S. diffuse emission.

The CANGAROO-I results for Vela obtained by Yoshikoshi et al. (1997) were based on the data taken in 1993, 1994, and 1995. The Vela pulsar region was also observed in 1997 with the recoated 3.8 m reflector and a TeV gamma-ray signal was again detected, at the  $4.1\sigma$  level (Yoshikoshi 1998). The 1997 data were later also analyzed by Dazeley et al. (2001), who reproduced the same signal as Yoshikoshi (1998) but cast doubt upon its gamma-ray-likeness. No signal was found within a  $2^\circ$  field of view centered on the pulsar position using gamma-ray selection criteria optimized *a priori* with their Monte Carlo simulations (Dazeley & Patterson 2001).

In response to these inconsistencies, we have reanalyzed CANGAROO-I data of PSR B1706–44, SN 1006, and Vela, including the data used in the previous analyses, with our best current knowledge. The following facts were not known or not fully considered in the previous analyses: (1) the effects of some noise produced by the electronic system were only discovered after the previous

publications; (2) details of the analyses of CANGAROO-I data had varied from source to source, and sometimes from data set to data set, without a common, consistent treatment based on the experience gained over the lifetime of the telescope; (3) improved calibration methods had not been applied to some old data; (4) although the fact that the acceptance for gamma rays is not uniform across the field of view was well understood, the effect on gamma-ray morphologies had not been investigated in detail; and (5) for Vela, a more precise energy spectrum, measured by H.E.S.S., is available now (Aharonian et al. 2006a) and the systematic uncertainty of the integral flux has been reduced. Our aim in this paper is to investigate these issues on the CANGAROO-I data in detail, although the information available on the previous analyses is, in places, limited. We briefly summarize the CANGAROO 3.8 m IACT and its specifications related to the analyses in Section 2, and then the data of the three objects are summarized in Section 3. The common and standard analysis method redefined considering the above problems is described in Section 4 in detail, and the results obtained with it are summarized in Section 5. Several issues on the old results such as reproducibility and reliability are discussed in Section 6, and we finally conclude in Section 7.

## 2. CANGAROO 3.8 M TELESCOPE

The CANGAROO 3.8 m IACT (Hara et al. 1993) was operated near Woomera, South Australia ( $136^\circ 47' \text{E}$ ,  $31^\circ 06' \text{S}$ , 160 m a.s.l.). The telescope detected Cherenkov photons from extensive air showers (EASs) generated by primary gamma rays and cosmic rays. The parabolic reflector of the telescope had both a diameter and a focal length of 3.8 m. The telescope was originally used for lunar ranging, and the reflectivity of its Kanigen-plated surface was about 45% at wavelengths of atmospheric Cherenkov light. The reflector was recoated with aluminum in 1996 October and its reflectivity improved to about 75%,<sup>15</sup> which deteriorated to about 55% by 1998. The reflectivity was monitored using a portable reflectometer (Dowden et al. 1997) with a systematic error of about 5%.

The telescope had an imaging camera of Hamamatsu R2248 square photomultiplier tubes (PMTs) in the focal plane. Observations started with 224 PMTs, which were increased to 256 PMTs in 1995 April by adding 34 PMTs at the corners of the camera. The number of PMTs decreased to 240 because of hardware trouble in 1998 February. Each PMT viewed an angular extent of  $0^\circ.12 \times 0^\circ.12$ , and the field of view of the camera was about  $3^\circ$  across with a  $0^\circ.18$  spacing between pixel centers. Light guides were used from 1995 November to capture Cherenkov photons otherwise incident on the dead space between photocathodes but abandoned in 1996 November owing to complications described later.

Outputs of the PMTs were fed into the electronics, consisting of trigger and data acquisition circuits after amplification by buffer amplifiers. The data acquisition circuits are based on analog-to-digital converters (ADCs), time-to-digital converters (TDCs), and scalers for indi-

<sup>14</sup> <http://www.mpi-hd.mpg.de/hfm/HESS/pages/home/som/2008/08/>.

<sup>15</sup> This value is the average of the whole surface and smaller than that of the recoated surface ( $\sim 80\%$ ) since only the outer part of the reflector was recoated.

TABLE 1  
SUMMARY OF THE CANGAROO-I DATA SETS USED IN THIS PAPER.

Target	Year	$T_{\text{ON}}^{\text{d}}$ (hr)	$T_{\text{OFF}}^{\text{d}}$ (hr)
PSR B1706–44	1993 <sup>a</sup>	66.9 (44.3)	50.3 (44.3)
	1994	19.4 (19.1)	19.6 (19.1)
	1995	33.9 (26.0)	28.4 (26.0)
	1997	24.1 (18.4)	19.8 (18.4)
	1998	44.2 (31.5)	35.0 (31.5)
Vela	1993 <sup>b</sup>	52.0 (32.6)	42.2 (32.6)
	1994 <sup>b</sup>	63.8 (41.9)	56.7 (41.9)
	1995 <sup>b</sup>	50.2 (44.9)	46.7 (44.9)
	1997	28.8 (16.6)	21.4 (16.6)
SN 1006	1996 <sup>c</sup>	26.8 (8.2)	14.7 (8.2)
	1997 <sup>c</sup>	34.7 (28.4)	29.6 (28.4)

<sup>a</sup> Used in Kifune et al. (1995). <sup>b</sup> Used in Yoshikoshi et al. (1997). <sup>c</sup> Used in Tanimori et al. (1998). <sup>d</sup> Observation time for ON-source (OFF-source) after rejecting periods affected by clouds or significant electronic noise. The number in brackets is the observation time after matching ON- and OFF-source observations in horizontal coordinates.

vidual PMTs, which record brightness and arrival timing of Cherenkov light, and brightness of night-sky background (NSB) light, respectively.

### 3. DATA

The CANGAROO-I data used in this paper are listed in Table 1. The data have been taken in ON/OFF mode, in which OFF-source data to estimate the background level are taken on the same night, but with an offset in right ascension, as the ON-source observation which included the target object in the field of view. The total observation times for ON- and OFF-source data in Table 1 ( $T_{\text{ON}}$  and  $T_{\text{OFF}}$ , respectively) are those after rejecting periods affected by clouds or significant electronic noise, which are determined from descriptions in logbooks and/or background event rates. The ON- and OFF-source data have further been matched in horizontal coordinates of the observations to make observation conditions as similar as possible, since some data were not taken following the above policy, and the corresponding observation times are given in brackets. In the following analyses, we use the data sets after matching ON- and OFF-source exposures unless otherwise specified.

The data used in the previous papers are indicated by the superscript marks in the year column in Table 1. PSR B1706–44 was also observed in 1992, and those data were used in the analysis of Kifune et al. (1995). However, they are not used here because some of the original data files have been lost and some necessary calibration data were not taken at that time, and it is expected that the performance over this first observing season will be more variable as problems were identified and addressed.

### 4. ANALYSES

Except where otherwise specified, a common analysis method is used for all data sets in this paper, since the nature of Cherenkov light images of EASs is independent of the observed object. In the previous CANGAROO-I papers, the analysis conditions differed for each object without a single, consistent underlying philosophy, in part as the understanding of the telescope improved with time. It is possible, however, to enhance an appar-

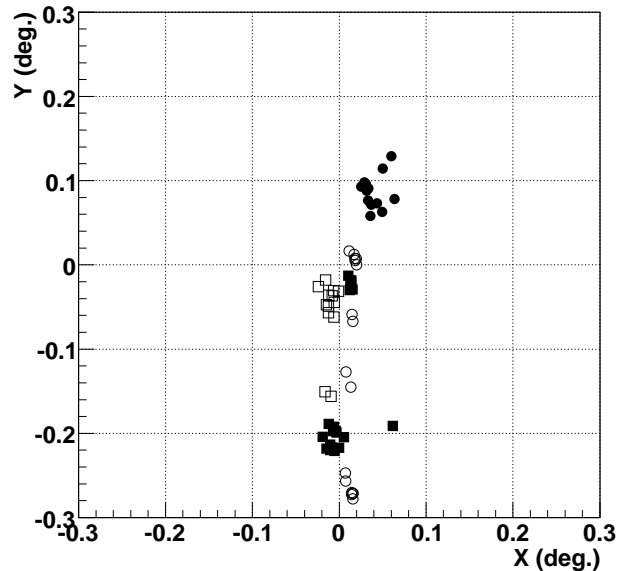


FIG. 1.— Calibrated tracking centers in the camera in the case of the Vela observations over five years. The origin is the center of the camera, and the Y-axis points to the zenith. Tracking centers of the 1993, 1994, 1995, and 1997 data are represented by solid circles, open circles, solid squares, and open squares, respectively.

ent signal by using some of the many degrees of freedom in reducing the background level. To reduce the degrees of freedom in the analyses and ensure the results are robust, we use here a simple analysis method similar to the “Supercuts” method of the Whipple group (Punch et al. 1991), which is described in Section 4.4.

#### 4.1. Calibration of Tracking Centers

The telescope tracking position in the field of the imaging camera is calibrated using the time variation of scaler counts of individual PMTs. When a bright star image is within the field of view of a PMT, its count rate increases. Since the telescope has an alt-azimuth mount, bright star images revolve around the center of the field of view of the camera, and the time profile of scaler counts shows peaks due to the passages of stars. The offset angle of the tracking direction from the center of the camera can be estimated by comparing the observed time profiles with simulated ones. It is necessary for this calibration to be done night by night as issues with the mount were found to sometimes result in offsets of greater than  $0^\circ.1$ , comparable to the size of the point-spread function (PSF). Figure 1 shows an example of tracking centers calibrated night by night in the case of the Vela observations over five years, in which the maximum difference between the vertical offsets is more than  $0^\circ.4$ . Details of the calibration procedure are given in Yoshikoshi (1996).

#### 4.2. Image Generation and Cleaning

The relative Cherenkov light signal of the  $i$ th pixel  $s_i$  is obtained using the following formula:

$$s_i = \frac{a_i - p_i}{g_i}, \quad (1)$$

where  $a_i$ ,  $p_i$ , and  $g_i$  are the ADC value, the ADC pedestal value, and the relative gain of the  $i$ th pixel, respectively.

The ADC pedestal value of each pixel is determined using Cherenkov light triggered events. After omitting any pixel which contains a signal or is adjacent to a pixel containing a signal, the ADC distribution of each pixel is fitted by a Gaussian distribution. The presence of a TDC signal is used to determine that a pixel contains a signal. The ADC pedestal value, taken to be the mean value of the Gaussian distribution, is subtracted from the ADC value. The pedestal standard deviation represents the noise level of the ADC value due to NSB light and electronic noise. Any PMT signal lower than the  $1\sigma$  threshold based on the noise level is rejected from the image. Pixel gains relative to their average are determined using LED data, which were taken by artificial triggers with a LED, permanently positioned at the front of the camera for flashing uniform light at the all PMTs, before or after Cherenkov light observation runs. Cherenkov light images are flat-fielded, i.e., divided by  $g_i$  as in equation (1).

Background levels of hadronic events estimated using OFF-source data are biased by the difference of NSB brightness between ON- and OFF-sources. Software padding (Cawley 1993) is an effective method to compensate for the difference, as demonstrated successfully by the Whipple group. We have tried to apply this method to some CANGAROO-I data sets, but did not find it to be effective. This is due to the fact that ADC signals have already been padded by electronic noise, which were generated only when high voltages were supplied to the PMTs, just like the original “hardware” padding utilized in most first-generation ACT systems (Fruin & Jelley 1968; Weekes et al. 1972; Cawley 1993). The other sources of noise described in the following sections have larger effects and parameter distributions of background events match reasonably well between ON- and OFF-source regions after considering them. Therefore, software padding is not used in this paper.

In 1997, we found that the discriminators which precede the TDCs and scalers generate noise when they are fired, significantly affecting the ADCs on the same circuit board. This results in inherent offsets in individual ADCs in such events. This “ADC offset” noise can however be measured by using the ADC itself and by setting discriminator thresholds to be very low compared to their normal values (typically three photoelectrons). In the most affected channels, the offsets amount to about 40 ADC counts, which correspond to about eight photoelectrons and thus distorts dimmer Cherenkov images significantly. We use the following formula to compensate for the ADC offset  $o_i$  instead of Equation (1):

$$s_i = \frac{a_i - p_i - o_i}{g_i}. \quad (2)$$

From the pixels remaining after the above selections, isolated pixels, which are not adjacent to any other pixels containing signals, are further removed to extract clusters in the image. This process was traditionally designed to remove effects of the NSB noise. The remaining pixels are used to define the image parameters described in Section 4.4.

#### 4.3. Rejection of Electronic Noise Events

The imaging camera consists of box units in which eight adjacent PMTs selected to have similar gains share

the same high voltage. In early data, in particular, noise events in which all eight PMTs in a box unit were simultaneously hit were frequently generated by the telescope drive system. These noise events, referred to as “box noise”, must be rejected as much as possible because they are compact and mimic gamma-ray events. We define a parameter  $b$  to reject box noise as follows:

$$b = \frac{\max_i n_i}{n}, \quad (3)$$

where  $n_i$  is the number of TDC hits in the  $i$ th box of eight PMTs and  $n$  is the total number of TDC hits in an image. The box noise events have large values of  $b$  close to (or equal to) its maximum value of 1. In the standard analysis here, events of  $b$  greater than 0.8 are rejected. This rejection is very effective unless two or more boxes are triggered in this way simultaneously, although small Cherenkov images are also somewhat reduced as a sacrifice. About 15% of reconstructed events are rejected with this cut on average, but the fraction can be larger depending on the noise level.

Using signals of the selected pixels, the image *size* (sum of the ADC values), the number of selected pixels (referred to as  $N_{\text{hit}}$  though it is not the true number of TDC hits), and the image centroid (first moment of the image) are calculated. Events of small *size* or  $N_{\text{hit}}$  are more affected by noise, and therefore events of *size* < 200 ADC counts or  $N_{\text{hit}}$  < 5 are rejected before the following imaging analysis. Also, images of the centroids more than  $1^\circ 05$  distant from the center of the camera are eliminated. This is called the “edge cut” since part of such an image has possibly been lost out of the camera edge, resulting in the image shape being distorted. On average, the *size*,  $N_{\text{hit}}$ , and edge cuts individually reject about 40%, 25%, and 55% of reconstructed events, respectively, and about 75% of reconstructed events are rejected by the three cuts applied all together.

#### 4.4. Imaging Analysis

The atmospheric Cherenkov imaging analysis is based on the Hillas parameters (Hillas 1985; Weekes et al. 1989; Reynolds et al. 1993), which are the second moments of light intensity both parallel (*length*) and perpendicular (*width*) to the major axis of the image, the light concentration of the two brightest pixels (*conc*), the distance of the image centroid from the source (*dis*), and the orientation angle with respect to the major axis (*alpha*). They are also referred to as shape (*width*, *length*, and *conc*), location (*dis*), and orientation (*alpha*) parameters. Images of gamma-ray-induced air showers tend to have smaller *width*, *length*, and *alpha*, and larger *conc* than background hadronic showers, reflecting the different profiles of shower development and different source distributions in the field of view. In the case of a point source, the signal-to-noise ratio is improved by more than an order of magnitude by applying selections for gamma-ray-like events to the parameter values.

The standard gamma-ray selection criteria used in this paper are simple and represented as follows:

$$\begin{aligned} \text{width} &\leq w_{\text{max}} \\ \text{length} &\leq l_{\text{max}} \\ c_{\text{min}} &\leq \text{conc} \\ d_{\text{min}} &\leq \text{dis} \leq d_{\text{max}} \\ \text{alpha} &\leq a_{\text{max}}. \end{aligned} \quad (4)$$

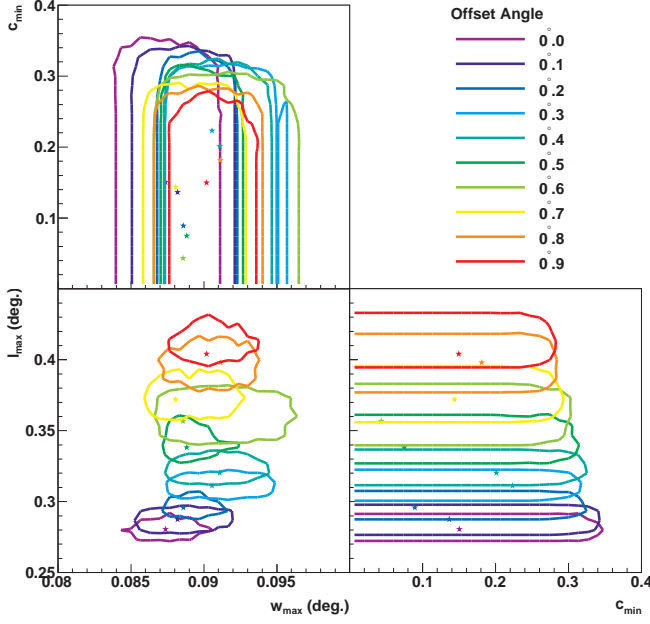


FIG. 2.— Correlations between the best gamma-ray selection criteria giving the maximum  $q$  factors in the case of the Vela 1993–1995 analysis. Bottom left:  $l_{\max}$  (upper limit for *length*) vs.  $w_{\max}$  (upper limit for *width*), top left:  $c_{\min}$  (lower limit for *conc*) vs.  $w_{\max}$ , and bottom right:  $c_{\min}$  vs.  $l_{\max}$ . The star marks indicate the best combinations of the selection criteria and the lines indicate their  $1\sigma$  error regions. The different colors indicate different offset angles of the source from the center of the camera with the  $0^\circ$ – $1^\circ$  interval.

The best combination of the upper and lower limits in the above selection criteria is determined so as to maximize the quality factor  $q$ :

$$q = \frac{\epsilon_\gamma}{\sqrt{\epsilon_{\text{BG}}}}, \quad (5)$$

where  $\epsilon_\gamma$  and  $\epsilon_{\text{BG}}$  are the efficiencies of the selection criteria for gamma-ray and background events, respectively. Gamma-ray event samples are generated using Monte Carlo simulations, and for background event samples actual OFF-source data are used. Only shape parameters, *width*, *length*, and *conc*, are used in the optimization because the distributions of location and orientation parameters depend on the source distribution that is not known *a priori*. Nevertheless, the best selection criteria on the shape parameters depend on the source position in the camera, especially on the offset angle of the source from the camera center, which can change night by night owing to the shift of the tracking center. The average offset angle is calculated in each data set and incorporated in the Monte Carlo simulations.

Figure 2 shows correlations between the best gamma-ray selection levels on the shape parameters with the OFF-source data of the Vela 1993, 1994, and 1995 observations used as the background samples. The best combination of  $w_{\max}$ ,  $l_{\max}$ , and  $c_{\min}$  for each offset angle of a point source from the camera center is indicated by a star mark, and the closed line around it represents the  $1\sigma$  error region, which is defined so that  $q \geq q_{\max} - \sigma_{q_{\max}}$ . It is clearly seen that the more distant the source position is from the camera center, the larger the upper limit to *length*  $l_{\max}$  is, but  $w_{\max}$  and  $c_{\min}$  are less dependent on the source offset. The relative errors of  $c_{\min}$  are larger than those of  $w_{\max}$  and  $l_{\max}$  since *conc* is correlated with

*width* and *length*. The positions of the best shape selection levels indicated by the star marks seem quite widely spread within the  $1\sigma$  error regions, especially for *conc*, since  $q$  is a discrete function of the selection levels by definition.

The best shape selection levels for individual data sets are listed in Table 2. For each data set,  $5 \times 10^5$  gamma-ray showers have been simulated, randomly injected into a circular area of 300 m radius around the telescope. Gamma-ray energies are also randomly selected in the range between 500 GeV and 100 TeV assuming that they follow a power-law differential spectrum or that with an exponential cutoff. The assumed spectral index and cut-off energy are listed in Table 3 together with the other input conditions in the simulations described in Section 2. The spectral index and cutoff energy for Vela are now known and taken from the reference given in the table, but the spectral indices for PSR B1706–44 and SN 1006 are assumed to be the Crab-like value of  $-2.5$ . The zenith angles of gamma-ray injections are selected near the culminations of the objects at which most events were observed. In spite of the various differences in the observation conditions, the best selection levels are consistent within the errors, of which the definition is the same as in Figure 2, except for the effect of the source offset from the camera center.

The optimization of selection levels on location and orientation parameters is complicated if the effect of source extent is considered. Instead, we here take just simple criteria: the *dis* limits are common as  $d_{\min} = 0.7^\circ$  and  $d_{\max} = 1.2^\circ$  since their dependence on the source extent is not so strong, and  $a_{\max} = 10^\circ$  for sources whose extent is comparable to the PSF, and for sources more extended the same ranges as used in the previous CANGAROO-I paper (Tanimori et al. 1998;  $\alpha \leq 15^\circ$ ) are adopted.

#### 4.5. Estimation of Integral Gamma-Ray Fluxes

The integral gamma-ray fluxes obtained in this paper have been estimated using the following formula:

$$F(> E_{\text{th}}) = \frac{N_{\text{excess}}}{N_{\text{expected}}} F_0(> E_{\text{th}}), \quad (6)$$

where  $E_{\text{th}}$  is the threshold energy for gamma rays, which is defined as the modal energy of selected gamma rays,  $N_{\text{excess}}$  is the number of excess events,  $F_0$  is the assumed integral gamma-ray flux from the source, and  $N_{\text{expected}}$  is the expected number of gamma rays represented as follows:

$$N_{\text{expected}} = A_0 \epsilon t \int_{E_{\min}}^{E_{\max}} f_0(E) dE, \quad (7)$$

where  $f_0 = -dF_0/dE$  is the assumed differential gamma-ray flux from the source,  $E_{\min}$  and  $E_{\max}$  are the minimum and maximum energies of gamma rays generated in the simulations, respectively,  $A_0 = \pi r_{\max}^2 \cos \theta$  is the area within which simulated gamma rays were injected, with the maximum horizontal distance between the telescope and the shower axis  $r_{\max} = 300$  m and the zenith angle  $\theta$ ,  $\epsilon$  is the acceptance defined as  $\epsilon = N_{\text{surviving}}/N_{\text{input}}$ , in which  $N_{\text{input}}$  and  $N_{\text{surviving}}$  are the numbers of input gamma rays and gamma rays surviving after the selections, respectively, and  $t$  is the observation time.

TABLE 2  
BEST GAMMA-RAY SELECTION CRITERIA FOR EACH DATA SET.

Target	Year	Offset <sup>a</sup>	$q_{\max}$	$w_{\max}$	$l_{\max}$	$c_{\min}$
PSR B1706-44	1993	0° 1	$1.549 \pm 0.012$	$0^\circ 0883^{+0^\circ 0046}_{-0^\circ 0036}$	$0^\circ 288^{+0^\circ 013}_{-0^\circ 007}$	$0.17^{+0.18}_{-0.17}$
	1994	0° 1	$1.567 \pm 0.015$	$0^\circ 0873^{+0^\circ 0057}_{-0^\circ 0033}$	$0^\circ 288^{+0^\circ 025}_{-0^\circ 008}$	$0.34^{+0.03}_{-0.34}$
	1995	0° 1	$1.563 \pm 0.014$	$0^\circ 0896^{+0^\circ 0026}_{-0^\circ 0049}$	$0^\circ 292^{+0^\circ 024}_{-0^\circ 012}$	$0.15^{+0.20}_{-0.15}$
	1997	0° 1	$1.748 \pm 0.016$	$0^\circ 0856^{+0^\circ 0052}_{-0^\circ 0058}$	$0^\circ 294^{+0^\circ 017}_{-0^\circ 011}$	$0.08^{+0.27}_{-0.08}$
	1998	0° 1	$1.995 \pm 0.025$	$0^\circ 0810^{+0^\circ 0047}_{-0^\circ 0044}$	$0^\circ 300^{+0^\circ 015}_{-0^\circ 026}$	$0.12^{+0.25}_{-0.12}$
Vela	1993, 1994, 1995	0° 2	$1.560 \pm 0.007$	$0^\circ 0886^{+0^\circ 0034}_{-0^\circ 0017}$	$0^\circ 296^{+0^\circ 012}_{-0^\circ 009}$	$0.09^{+0.25}_{-0.09}$
		0° 4	$1.466 \pm 0.006$	$0^\circ 0911^{+0^\circ 0035}_{-0^\circ 0040}$	$0^\circ 320^{+0^\circ 016}_{-0^\circ 010}$	$0.20^{+0.13}_{-0.20}$
	1997	0° 1	$1.635 \pm 0.008$	$0^\circ 0929^{+0^\circ 0037}_{-0^\circ 0066}$	$0^\circ 296^{+0^\circ 016}_{-0^\circ 009}$	$0.23^{+0.10}_{-0.23}$
		0° 4	$1.482 \pm 0.007$	$0^\circ 0953^{+0^\circ 0036}_{-0^\circ 0058}$	$0^\circ 331^{+0^\circ 028}_{-0^\circ 014}$	$0.10^{+0.22}_{-0.10}$
SN 1006	1996	0° 3	$1.557 \pm 0.022$	$0^\circ 0962^{+0^\circ 0032}_{-0^\circ 0033}$	$0^\circ 309^{+0^\circ 025}_{-0^\circ 012}$	$0.23^{+0.08}_{-0.23}$
		0° 7	$1.413 \pm 0.018$	$0^\circ 0957^{+0^\circ 0029}_{-0^\circ 0041}$	$0^\circ 393^{+0^\circ 028}_{-0^\circ 065}$	$0.15^{+0.13}_{-0.15}$
	1997	0° 3	$1.555 \pm 0.010$	$0^\circ 0924^{+0^\circ 0030}_{-0^\circ 0063}$	$0^\circ 321^{+0^\circ 014}_{-0^\circ 021}$	$0.13^{+0.21}_{-0.13}$

<sup>a</sup> Offset angle of the source from the center of the camera.

TABLE 3  
INPUT CONDITIONS IN THE MONTE CARLO SIMULATIONS FOR EACH DATA SET.

Target	Year	Spectral Index	Cutoff Energy (TeV)	Zenith Angle (deg)	Light Guide	Reflectivity (%)	Number of PMTs
PSR B1706-44	1993	-2.5	...	15	no	45	224
	1994	-2.5	...	15	no	45	224
	1995	-2.5	...	15	no	45	256
	1997	-2.5	...	15	no	75	256
	1998	-2.5	...	15	no	55	240
Vela	1993, 1994, 1995	-1.45 <sup>a</sup>	13.8 <sup>a</sup>	15	no	45	224
		-1.45 <sup>a</sup>	13.8 <sup>a</sup>	15	no	75	256
SN 1006	1996	-2.5	...	10	yes	45	256
	1997	-2.5	...	10	no	75	256

<sup>a</sup> Aharonian et al. (2006a).

## 5. RESULTS

The numbers of events remaining after the selections described above are summarized in Table 4 for all data sets used in this paper. The selections listed in the table header have cumulatively been applied to each data set from left to right. The statistical significances of the excess events obtained after applying all selections have been calculated using the formula obtained by Li & Ma (1983) utilizing the likelihood ratio. Note that after the noise rejections the numbers of ON- and OFF-source events match with each other within a few percent except for the 1998 PSR B1706-44 data. Details are given in the following subsections.

### 5.1. PSR B1706-44

The five data sets of PSR B1706-44 have been reanalyzed separately since the 1993 data used in the previous CANGAROO-I paper should independently be analyzed for comparison, and the mirror reflectivities and camera configurations of the other data sets listed in Table 1 all differ. The average offset of the object from the camera center is about 0°1, which has been assumed to be common for all data sets. The gamma-ray selection crite-

ria listed in Table 2 are optimized for this common offset, but the selection levels are different from data set to data set since the OFF-source data of each data set have been used as the background samples in each optimization.

The  $\alpha$  distributions of ON- and OFF-source events remaining after the standard selections have been plotted for individual data sets in Figure 3. No statistically significant excess of ON-source events has been found near  $\alpha = 0^\circ$  in any data set, and the significant excess from the 1993 data previously reported has not been reproduced in this analysis. The ON- and OFF-source  $\alpha$  distributions of each data set agree well except for the 1998 data, in which the ON-source distribution is somewhat higher than the OFF-source distribution in the whole range. A possible reason for this is a temporary decrease of the mirror reflectivity due to dew condensation since it was humid in this period and more OFF-source data was taken in the hours before dawn. This diffuse excess is not gamma-ray-like considering the distributions of the shape parameters of the excess events, and a conservative upper limit is calculated here leaving the background mismatch as it is. Setting  $a_{\max} = 10^\circ$  for a relatively point-like source and assuming a Crab-

TABLE 4  
SUMMARY OF NUMBERS OF EVENTS REMAINING AFTER VARIOUS SELECTIONS.

Target	Year	ON/OFF	Raw <sup>a</sup>	Noise <sup>b</sup>	Shape <sup>c</sup>	Location <sup>d</sup>	Orientation <sup>e</sup> ( $a_{\max}$ )	Excess	Significance
PSR B1706-44	1993	ON	180105	57587	14942	8669	1090 (10°)	-67	-1.4 $\sigma$
		OFF	167397	56085	14570	8469	1157 (10°)		
	1994	ON	62616	20602	5014	2763	366 (10°)	-24	-0.9 $\sigma$
		OFF	63818	21186	5094	2863	390 (10°)		
	1995	ON	159487	19865	4454	2445	299 (10°)	-31	-1.2 $\sigma$
		OFF	138384	20508	4775	2664	330 (10°)		
	1997	ON	114862	22541	3736	1994	230 (10°)	-2	-0.1 $\sigma$
		OFF	112291	22651	3792	2062	232 (10°)		
	1998	ON	91547	18662	2422	1280	160 (10°)	22	1.3 $\sigma$
		OFF	84319	16972	2082	1090	138 (10°)		
Vela	1993, 1994, 1995	ON <sup>f</sup>	420310	119974	29710	16970	2343 (10°)	298	4.5 $\sigma$
		OFF <sup>f</sup>	400418	120206	28867	16512	2045 (10°)		
		ON <sup>g</sup>	420310	119974	35190		10122 <sup>j</sup>	501	3.6 $\sigma$
		OFF <sup>g</sup>	400418	120206	34243		9621 <sup>j</sup>		
	1997	ON <sup>f</sup>	142158	36064	8039	4421	589 (10°)	84	2.5 $\sigma$
		OFF <sup>f</sup>	132171	35292	8004	4309	505 (10°)		
		ON <sup>g</sup>	142158	36064	9862		2624 <sup>j</sup>	75	1.0 $\sigma$
		OFF <sup>g</sup>	132171	35292	9772		2549 <sup>j</sup>		
	1996	ON <sup>h</sup>	33524	2105	564	216	32 (15°)	-5	-0.6 $\sigma$
		OFF <sup>h</sup>	27171	2122	581	213	37 (15°)		
		ON <sup>i</sup>	33524	2105	696	274	46 (15°)	2	0.2 $\sigma$
		OFF <sup>i</sup>	27171	2122	728	266	44 (15°)		
	1997	ON <sup>h</sup>	231398	57143	13572	6915	1246 (15°)	-94	-1.8 $\sigma$
		OFF <sup>h</sup>	226916	57112	14016	7199	1340 (15°)		

<sup>a</sup> Number of reconstructed events (at least two adjacent pixels containing signals). <sup>b</sup> Number of events remaining after the noise rejection described in Section 4.3 and the discharge noise rejection described in Section 5.2 for the SN 1006 1996 data. <sup>c</sup> Number of events remaining after the shape selections based on *width*, *length*, and *conc*. <sup>d</sup> Number of events remaining after the location selection based on *dis*. <sup>e</sup> Number of events remaining after the orientation selection based on *alpha*. <sup>f</sup> Analyzed with respect to the CANGAROO-I position ( $\alpha = 8^{\text{h}}35^{\text{m}}42^{\text{s}}$ ,  $\delta = -45^{\circ}17'$  (J2000)). <sup>g</sup> Analyzed with respect to HESS J0835-455 ( $\alpha = 8^{\text{h}}35^{\text{m}}00^{\text{s}}$ ,  $\delta = -45^{\circ}36'$  (J2000)). <sup>h</sup> Analyzed with respect to the NE rim with the selection criteria optimized for the source offset by  $0^{\circ}3$  from the camera center. <sup>i</sup> Analyzed with respect to the NE rim with the selection criteria optimized for the source offset by  $0^{\circ}7$  from the camera center. <sup>j</sup> Selected so that the arrival direction obtained using the source PDF method (Yoshikoshi 1996) is within the angular distance of  $0^{\circ}8$  from HESS J0835-455.

like spectral index of  $-2.5$  in the simulations, the upper limits to the integral fluxes at the 95% confidence level (CL) have been estimated using the method described in Section 4.5 and the method of Protheroe (1984). The results are as follows:

$$F_{93}(> 3.2 \pm 1.6 \text{ TeV}) < 8.03 \times 10^{-13} \text{ photons cm}^{-2} \text{ s}^{-1},$$

$$F_{93-94}(> 3.2 \pm 1.6 \text{ TeV}) < 6.06 \times 10^{-13} \text{ photons cm}^{-2} \text{ s}^{-1},$$

$$F_{95}(> 3.2 \pm 1.6 \text{ TeV}) < 8.85 \times 10^{-13} \text{ photons cm}^{-2} \text{ s}^{-1},$$

$$F_{97}(> 1.8 \pm 0.9 \text{ TeV}) < 4.08 \times 10^{-12} \text{ photons cm}^{-2} \text{ s}^{-1},$$

$$F_{98}(> 2.7 \pm 1.4 \text{ TeV}) < 1.29 \times 10^{-12} \text{ photons cm}^{-2} \text{ s}^{-1},$$

where  $F_{93-94}$  is the integral flux calculated adding the 1993 and 1994 data sets in which the observation conditions are the same. The different threshold energies for the above upper limits are mostly due to the different mirror reflectivities listed in Table 3. The errors of the threshold energies are systematic errors, defined in the same way as described by Muraishi et al. (2000). In the calculation of the flux upper limit of the 1997 data, only 7.9 hr of the ON- and OFF-source data, which corresponds to 43% of the data used elsewhere, have been used since blue optical filters were tested in the rest of the observations and their effect has not accurately been determined. The upper limits are plotted in Figure 4. They are higher than, and therefore not inconsistent with, the H.E.S.S. upper limits reported by Aharonian et al. (2005a).

## 5.2. SN 1006

The SN 1006 data taken in 1996 and 1997 have been analyzed with respect to the northeast (NE) rim ( $\alpha = 15^{\text{h}}03^{\text{m}}54^{\text{s}}$ ,  $\delta = -41^{\circ}45'30''$  (J2000)), from which Tanimori et al. (1998) have claimed the detection of TeV gamma rays. The observations were made with average offsets of  $0^{\circ}3$  (June 1996 and 1997) and  $0^{\circ}7$  (1996 April) of the NE rim from the camera center in order to move the bright star  $\beta$  Lup (magnitude 2.68) out of the field of view of the camera. Because of these relatively large offsets, the best gamma-ray selection criteria for SN 1006 listed in Table 2 are looser than the others following the tendency indicated in Figure 2. In the case of the 1996 data, the looser criteria are also caused by the light guides<sup>16</sup> which were used only in this period. In the case of CANGAROO-I, the collection efficiency of the light guides is thought to be worse than originally expected owing to difficulties in placing them in proximity to the photocathodes which resulted in discharge noise generated between the light guides and photocathodes, and the Cherenkov event rate in fact decreased after their installation. Here, to generate simulation events, we assume the light guide efficiency to be 45%, which is almost the same as the filling factor of the photocathodes. As in the case of PSR B1706-44, the Crab-like spectral index  $-2.5$  is assumed in the simulations.

<sup>16</sup> Light guides are utilized to detect Cherenkov photons otherwise incident on the gaps between photocathodes of PMTs but at the same time serve to somewhat smear Cherenkov images.

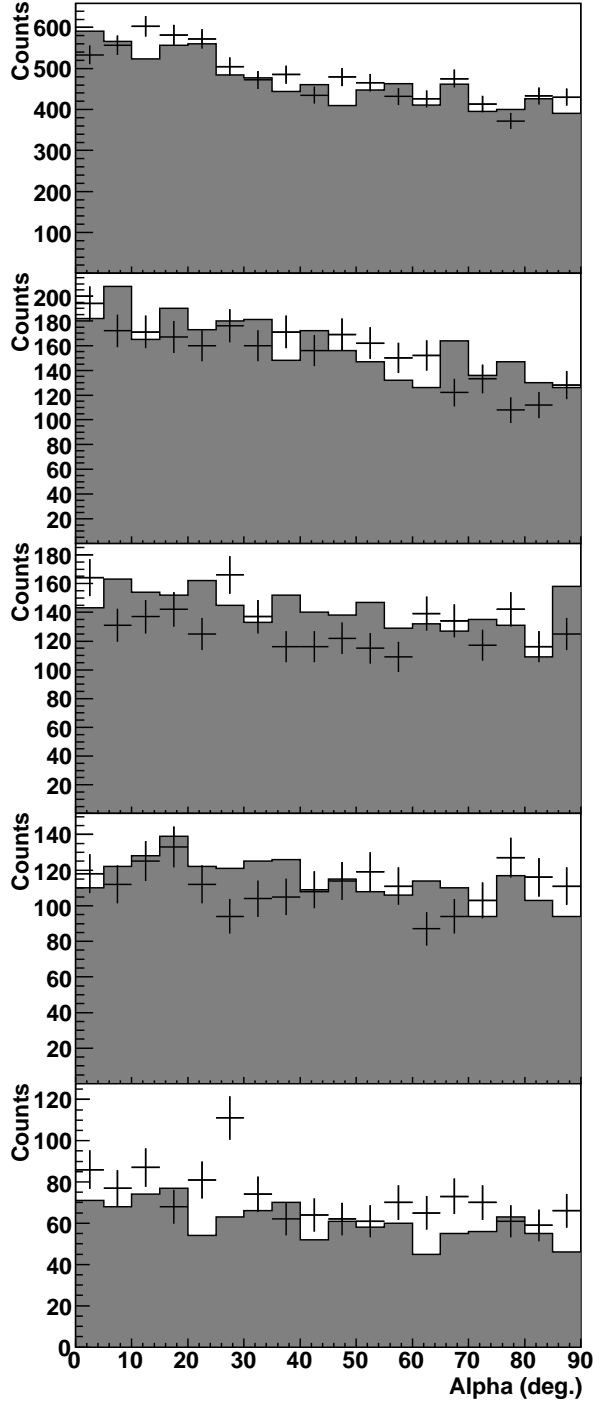


FIG. 3.— Distributions of the orientation parameter  $\alpha$  for the PSR B1706-44 data sets. From the top: distributions of the 1993, 1994, 1995, 1997, and 1998 data. The histograms with error bars are the ON-source distributions, and the gray solid histograms are the OFF-source distributions.

As mentioned above, the 1996 data were contaminated by discharge noise, in which the hardware trigger rate suddenly increased, especially in humid conditions, with only one or two PMTs having very large ADC values in one image. Such images are compact and have large sizes, and therefore, mimic gamma-ray images. We here take the following simple method to reject the discharge noise events.

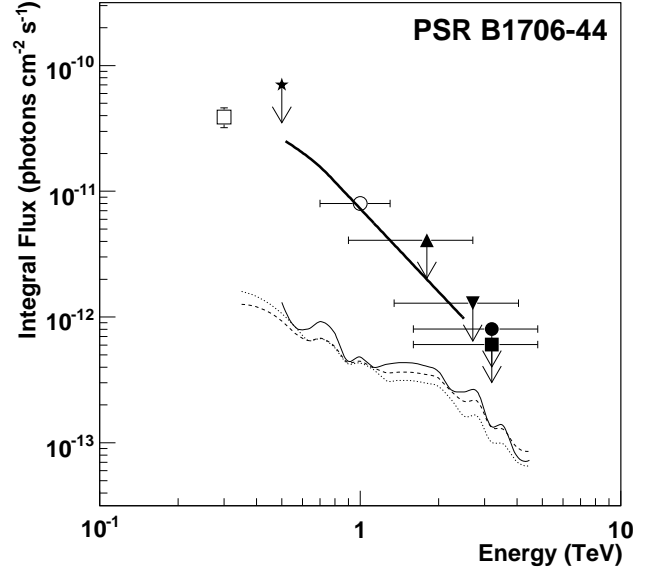


FIG. 4.— Integral gamma-ray fluxes from PSR B1706-44 obtained using the CANGAROO-I data. The 95% CL upper limits to the integral flux from PSR B1706-44 obtained from the 1993, 1993 + 1994, 1997, and 1998 data are indicated by the filled circle, filled square, filled triangle, and filled upside-down triangle, respectively. The open circle indicates the integral flux estimated by Kifune et al. (1995) using the 1993 data. The horizontal bars represent the systematic errors of the threshold energies. The 99% CL upper limit curves obtained by H.E.S.S. (Aharonian et al. 2005a) are indicated by the thin solid, dashed, and dotted lines. The thick solid line is the integral spectrum converted from the preliminary CANGAROO-II result (Kushida et al. 2003). The open square and filled star indicate the results from Chadwick et al. (1998) and Rowell et al. (1998), respectively.

1. For each pixel, the rate in which the pixel has the maximum ADC value in the image is calculated.
2. Pixels with rates higher than 0.01 Hz are marked as noisy pixels night by night (the rate of normal pixels is about 0.001 Hz).
3. Discharge noise events are identified and rejected if the pixel having the maximum ADC value in the image coincides with one of the marked pixels for the night.

This discharge noise cut is more robust than the old method described in Section 6.2 and more than 75% of shower events remain after this cut. The numbers of ON- and OFF-source events after the cut match quite well and the difference between them is only 0.8%.

The 1997 data are free from the discharge noise since the light guides were removed in 1996 November. However, the number of ON-source events after the other noise cuts described in Section 4.3 is more than a few percent larger than that of OFF-source events. This mismatch is probably due to the difference of brightness in the field of view between ON- and OFF-sources since another bright star,  $\kappa$  Cen (magnitude 3.13), was inevitably included in the ON-source field of view. To reduce the effect of bright stars, pixels having scaler values greater than  $100 \text{ counts ms}^{-1}$  were removed from the image in the analysis of the 1997 data. As a result, the numbers of ON- and OFF-source events match quite well as shown in Table 4.



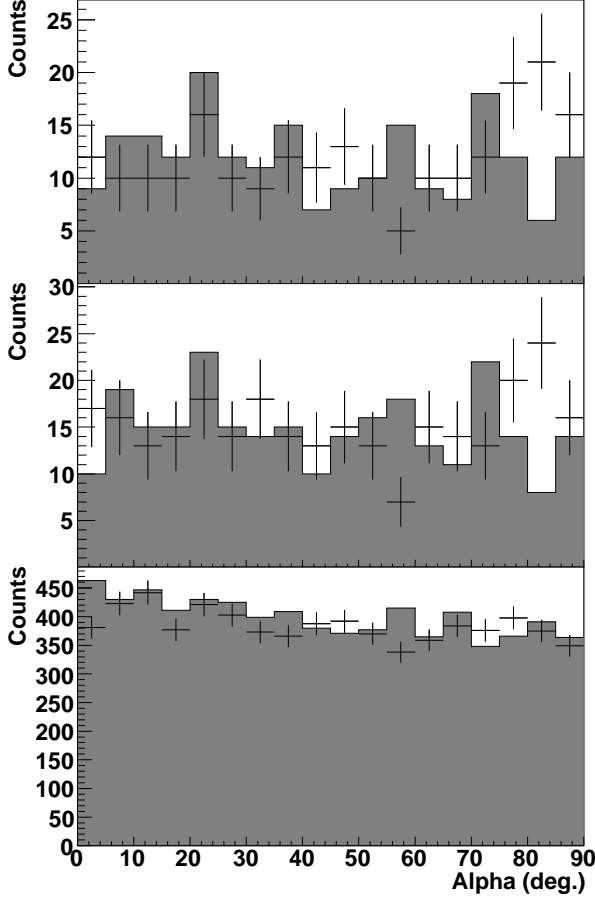


FIG. 5.— Distributions of the orientation parameter  $\alpha$  for the SN 1006 data sets. The  $\alpha$  values have been calculated with respect to the NE rim of the SNR. Top: distributions of the 1996 data with the best selection criteria optimized for the  $0.3^\circ$  offset from the camera center, middle: distributions of the 1996 data with the best selection criteria for the  $0.7^\circ$  offset, and bottom: distributions of the 1997 data with the best selection criteria for the  $0.3^\circ$  offset. The histograms with the error bars and the gray solid histograms are ON- and OFF-source distributions, respectively.

Figure 5 shows the  $\alpha$  distributions of the SN 1006 data sets. No statistically significant gamma-ray signal has been found around  $\alpha = 0^\circ$  from the 1996 and 1997 data for both  $0.3^\circ$  and  $0.7^\circ$  offsets from the camera center. Therefore, the previous CANGAROO-I results have not been reproduced in this analysis. Setting  $\alpha_{\max} = 15^\circ$ , which is the same definition as used by Tanimori et al. (1998), the 95% CL upper limits to the integral flux have been calculated as follows:

$$F_{96,0.3}(> 3.0 \pm 1.5 \text{ TeV}) < 1.20 \times 10^{-12} \text{ photons cm}^{-2} \text{ s}^{-1},$$

$$F_{96,0.7}(> 3.0 \pm 1.5 \text{ TeV}) < 2.44 \times 10^{-12} \text{ photons cm}^{-2} \text{ s}^{-1},$$

$$F_{97,0.3}(> 1.8 \pm 0.9 \text{ TeV}) < 1.96 \times 10^{-12} \text{ photons cm}^{-2} \text{ s}^{-1}.$$

The difference between the threshold energies is mostly due to the different mirror reflectivities listed in Table 3. The errors of the threshold energies are systematic errors, as defined by Muraishi et al. (2000). These upper limits are plotted in Figure 6. They are higher than and not inconsistent with the H.E.S.S. upper limits on the SN 1006 flux (Aharonian et al. 2005b).

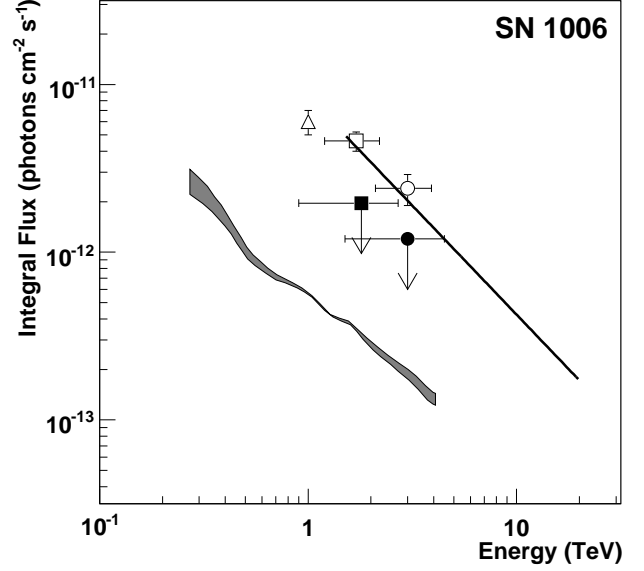


FIG. 6.— Integral gamma-ray fluxes from the NE rim of SN 1006 obtained using the CANGAROO-I data. The 95% CL upper limits to the integral fluxes are indicated by the filled circle (1996 data with the selection criteria optimized for the  $0.3^\circ$  offset) and the filled square (1997 data). The open circle and open square are the integral fluxes estimated by Tanimori et al. (1998) using the 1996 and 1997 data, respectively. The thick solid line is the integral spectrum converted from the CANGAROO-I differential spectrum (Tanimori et al. 2001). The horizontal bars represent the systematic errors of the threshold energies. The 99.9% CL upper limits obtained by H.E.S.S. (Aharonian et al. 2005b) are indicated by the gray band for a range of assumed photon indices (2–3). The open triangle indicates the preliminary CANGAROO-II result (Hara et al. 2001).

### 5.3. Vela

The analysis procedure has been applied to the Vela data, first with respect to the CANGAROO-I position ( $\alpha = 8^{\text{h}}35^{\text{m}}42^{\text{s}}$ ,  $\delta = -45^\circ 17'$  (J2000)), which is  $0.13^\circ$  offset from the Vela pulsar to the southeast (Yoshikoshi et al. 1997). The 1993–1995 data and 1997 data have been analyzed separately since the mirror reflectivity was improved in 1996. The average offsets of the object from the camera center are about  $0.2^\circ$  (1993–1995) and  $0.1^\circ$  (1997), for which the shape selection criteria listed in Table 2 have been optimized. The obtained  $\alpha$  distributions are shown in Figure 7. Setting  $\alpha_{\max} = 10^\circ$ , the statistical significances of the 1993–1995 data and 1997 data are  $4.5\sigma$  and  $2.5\sigma$ , respectively. The former is smaller than the previous result of  $5.2\sigma$  (Yoshikoshi et al. 1997), but the signal is still at a significant level. Note, however, that the CANGAROO-I position was found in the previous analysis after searching for the highest peak in the  $2^\circ \times 2^\circ$  area around the Vela pulsar (Yoshikoshi et al. 1997), and therefore the above values are “pre-trial” statistical significances.

Considering the  $0.18^\circ$  PSF (half width at half maximum) of CANGAROO-I (Yoshikoshi et al. 1997), the CANGAROO-I position does not coincide with the peak position of HESS J0835–455 detected by H.E.S.S., which is shown at the top left of Figure 8 (Aharonian et al. 2006a). However, the acceptance  $\epsilon$  is not uniform over the field of view and the morphology could significantly be distorted by this non-uniformity, especially for the

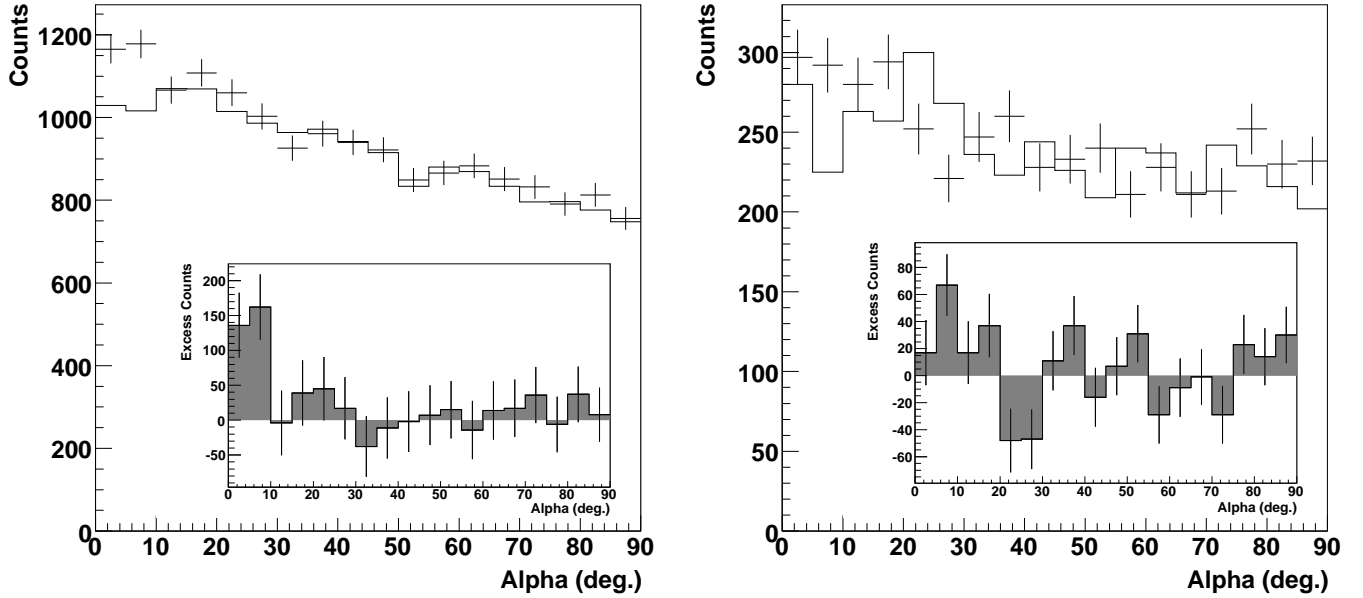


FIG. 7.— Distributions of the orientation parameter  $\alpha$  for the Vela data. The  $\alpha$  values have been calculated with respect to the CANGAROO-I position that is offset by  $0^\circ 13$  from the Vela pulsar to the southeast. The left and right figures have been obtained from the 1993–1995 data and the 1997 data, respectively. The ON- and OFF-source distributions are represented by the histograms with the error bars and the solid histograms, respectively. The histograms in the insets are the distributions of excess counts.

CANGAROO-I imaging camera which had a relatively small field of view, about  $3^\circ$  across. The top right of Figure 8 is the averaged acceptance distribution in the Vela pulsar region for the 1993–1995 observation period, obtained considering the night-by-night shifts of the tracking center in the camera and rotation of the camera with respect to the sky view due to the alt-azimuth mount. The expected morphology for CANGAROO-I is obtained from the H.E.S.S. morphology reweighted according to the CANGAROO-I acceptance and is shown at the bottom left of Figure 8, where the acceptance distribution of H.E.S.S. (Aharonian et al. 2006b) has not been considered but is almost uniform within the field of view compared to the CANGAROO-I acceptance. In this acceptance-reweighted morphology, the head of the “seahorse” shape, which corresponds to the CANGAROO-I source as shown in the bottom right of Figure 8, is more emphasized than in the original one. The CANGAROO-I morphology is obtained using the source probability density function (PDF) method (Yoshikoshi 1996), in which a PDF for the source position with respect to the image centroid, major axis, and *asymmetry* (Punch 1993; Yoshikoshi 1996) is defined using Monte Carlo simulations and a source distribution is made by adding up all PDFs of gamma-ray-like events. The angular distance between the peak of the acceptance-reweighted H.E.S.S. morphology and the CANGAROO-I position is  $0^\circ 05$ , which is comparable to the  $1\sigma$  error of the CANGAROO-I position  $\sim 0^\circ 04$  (Yoshikoshi 1996). Therefore, the TeV gamma-ray signal detected by CANGAROO-I is possibly part of HESS J0835–455. However, the above acceptance-reweighted morphology is still more extended than the CANGAROO-I source. This is possibly due to the energy dependence of the gamma-ray morphology: the threshold energy of the H.E.S.S. observations of Vela is 450 GeV which is an order of magnitude lower than

that of CANGAROO-I (see Section 6.3 for further discussion).

The integral flux from HESS J0835–455 has been estimated using the method described in Section 4.5. This H.E.S.S. source is diffuse extending up to the radius of  $0^\circ 8$  centered on position II ( $\alpha = 8^h 35^m 00^s$ ,  $\delta = -45^\circ 36'$  (J2000)) defined by Aharonian et al. (2006a). The *dis* and *alpha* cuts are not useful to estimate the flux of the same circular area as used by H.E.S.S., and instead we must estimate the arrival direction of each event as in the case of stereoscopic observations. Here, we estimate the arrival direction as the most probable point of the source PDF described above. The best gamma-ray selection criteria have been obtained for the position offset by  $0^\circ 4$  from the camera center since the position of the maximum emission of HESS J0835–455 is located around it on average. Simulation events have been generated with a power-law spectrum of the index of  $-1.45$  and an exponential cutoff at 13.8 TeV (Aharonian et al. 2006a). In the case of the 1993–1995 data, the numbers of ON- and OFF-source gamma-ray-like events falling into the circular area are 10,122 and 9621, respectively. The excess of 501 events corresponds to  $3.6\sigma$ , which is less significant than that for the CANGAROO-I position, owing to the inclusion of more background events in the extended area. The acceptance  $\epsilon$  depends on the source distribution in the field of view, but first we simply assume that the source is uniformly distributed in the circular area and  $\epsilon$  is averaged over it. The integral flux from HESS J0835–455 ( $0^\circ 8$  radius centered on position II) has thus been obtained as follows:

$$F_{93-95}(> 4.0 \pm 1.6 \text{ TeV}) = (3.28 \pm 0.92) \times 10^{-12} \text{ photons cm}^{-2} \text{ s}^{-1}.$$

The stated error in the threshold energy is the systematic error, as defined by Muraishi et al. (2000) except

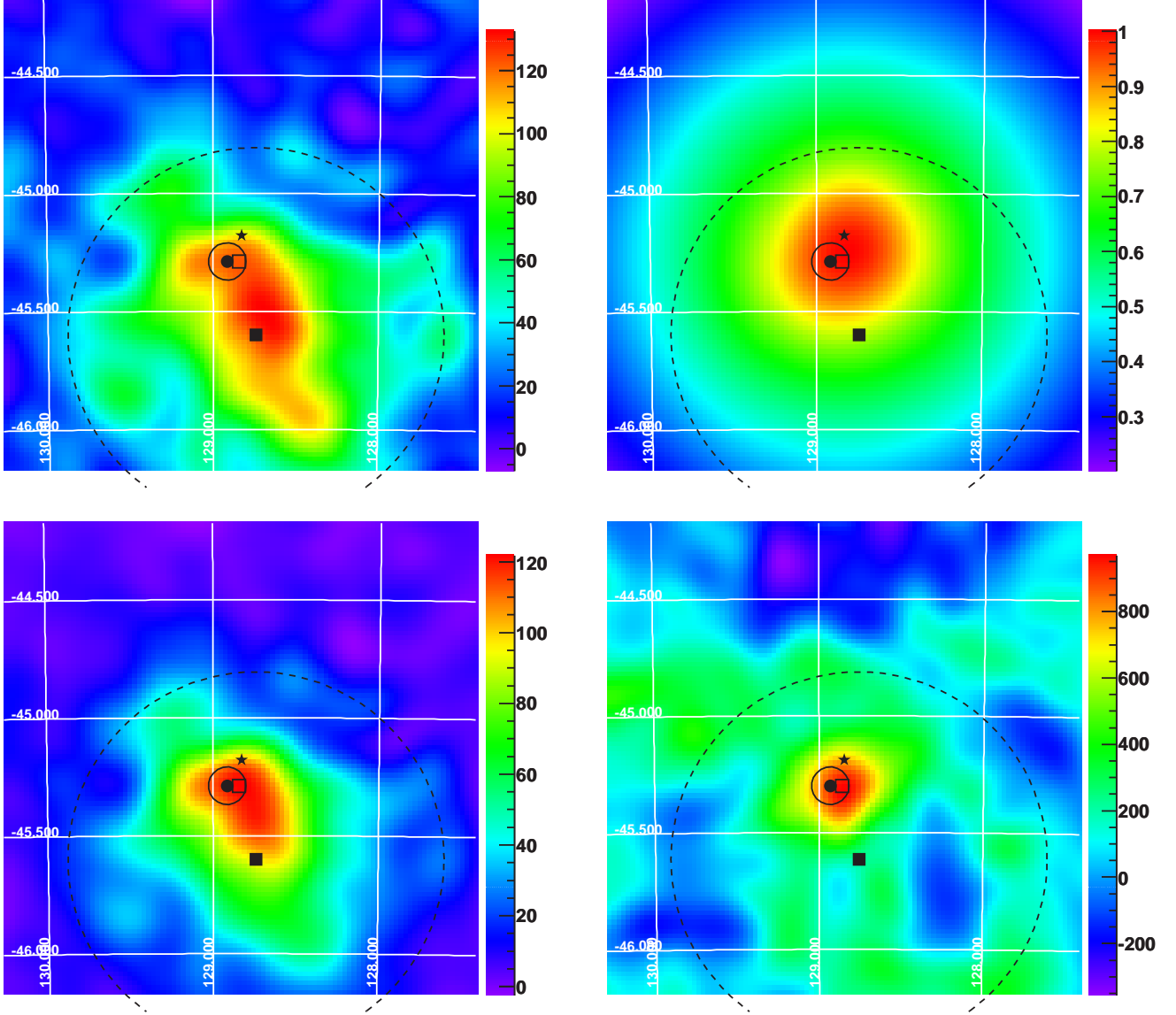


FIG. 8.— Sky maps of the Vela pulsar region. Top left: distribution of excess counts obtained by H.E.S.S. with the threshold energy of 450 GeV (Aharonian et al. 2006a), top right: averaged acceptance distribution in the CANGAROO-I observations from 1993 to 1995 normalized so that the maximum value is equal to 1, bottom left: H.E.S.S. excess distribution reweighted according to the CANGAROO-I acceptance, where the H.E.S.S. acceptance (Aharonian et al. 2006b) has not been considered but is almost uniform within the field of view compared to the CANGAROO-I acceptance, bottom right: distribution of excess counts obtained by CANGAROO-I with the threshold energy of 4 TeV using the source PDF method (Yoshikoshi 1996), in which the PSF size is  $0^\circ 18$  (half width at half maximum). The rainbow scales at the right are in counts per  $0^\circ 02 \times 0^\circ 02$  area for the H.E.S.S. distributions and in counts  $\text{deg}^{-2}$  for the CANGAROO distribution. The star mark at the center of each sky map indicates the position of the Vela pulsar. The filled circle indicates the peak position of the CANGAROO-I excess, whereas the filled and open squares indicate the position of the center of gravity of the H.E.S.S. excess and the peak position of the acceptance-reweighted H.E.S.S. excess, respectively. The small open circle around the CANGAROO-I position represents the  $2\sigma$  location error ( $1\sigma \sim 0^\circ 04$ ). The big dashed circle of the  $0^\circ 8$  radius indicates the integration region for HESS J0835–455 defined by H.E.S.S. (Aharonian et al. 2006a).

for the uncertainty of the spectral index, whereas the error of the flux is only statistical. The threshold energy of 4.0 TeV is higher than the previous estimation of 2.5 TeV (Yoshikoshi et al. 1997), owing to the harder spectrum used in the simulations this time. For HESS J0835–455, the two-dimensional Gaussian profile of the diffuse emission has been given by H.E.S.S. The average acceptance can more realistically be calculated using this profile, as weights and the integral flux obtained using this accep-

tance is

$$F_{93-95,G}(> 4.0 \pm 1.6 \text{ TeV}) = (3.05 \pm 0.86) \times 10^{-12} \text{ photons cm}^{-2} \text{ s}^{-1}.$$

The difference between the above two fluxes is small and well within the statistical errors.

The same calculation has been done also for the 1997 data: 2624 ON-source and 2549 OFF-source events remained after the selections and the excess of 75 events corresponds to  $1.0\sigma$ . Since this excess is not statistically significant, the 95% CL upper limits to the integral flux

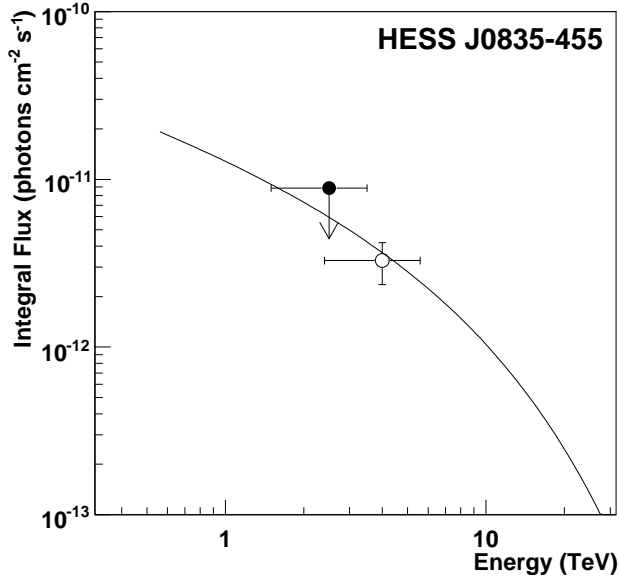


FIG. 9.— Integral gamma-ray fluxes from the Vela pulsar region ( $0^{\circ}8$  radius centered on HESS J0853–455) obtained from the CANGAROO-I data. The open circle represents the integral flux from the 1993 to 1995 data, and the filled circle represents the 95% CL upper limit to the flux from the 1997 data. The horizontal bars represent the systematic errors of the threshold energies. The solid line is the integral spectrum converted from the differential spectrum of HESS J0853–455 measured by H.E.S.S. assuming a power law with an exponential cutoff (Aharonian et al. 2006a).

have been calculated as follows:

$$F_{97}( > 2.5 \pm 1.0 \text{ TeV} ) < 8.87 \times 10^{-12} \text{ photons cm}^{-2} \text{ s}^{-1},$$

$$F_{97,G}( > 2.5 \pm 1.0 \text{ TeV} ) < 8.33 \times 10^{-12} \text{ photons cm}^{-2} \text{ s}^{-1}.$$

These fluxes are plotted in Figure 9 as well as the integrated H.E.S.S. spectrum (Aharonian et al. 2006a). The estimated fluxes are all consistent with the H.E.S.S. spectrum within statistical errors.

## 6. DISCUSSION

The results of the reanalyses described in the previous section are consistent with the recent H.E.S.S. results except for the morphological difference in the Vela pulsar region, which is possibly due to the difference of the threshold energy between the two experiments. In other words, the previous CANGAROO-I results for PSR B1706–44 and SN 1006 claiming the significant detections of TeV gamma rays have not been reproduced in the reanalyses. Therefore, we have tried to apply the same analysis methods as used before to the PSR B1706–44 and SN 1006 data to determine why the old gamma-ray signals were obtained, although not all details of the original analysis are still available.

### 6.1. Reproducibility of the Old PSR B1706–44 Results

Details of the analysis used to obtain the old PSR B1706–44 results are not given in the paper by Kifune et al. (1995). Therefore, we have used the analysis method described by Tamura et al. (1994) instead. The known differences of the method from the standard analysis described in Section 4 are listed below.

1. Some noise cut levels are different:  $size \geq 100$ ,  $N_{hit} \geq 4$ , and  $b$  (box noise parameter)  $\leq 0.7$ .

2. The gamma-ray selection criteria were defined as follows:

$$\begin{aligned} 0^{\circ}01 &\leq width \leq 0^{\circ}14 + 0^{\circ}045 \frac{size}{1500} \\ 0^{\circ}1 &\leq length \leq 0^{\circ}6 \\ length &\leq 0^{\circ}2 + 0^{\circ}4 \frac{size}{1500} \\ 0^{\circ}2 &\leq dis \leq 0^{\circ}96 \\ length &\leq dis \\ alpha &\leq 6^{\circ}75. \end{aligned}$$

In the old analysis, the above conditions were applied only to the PSR B1706–44 data taken in 1993 August, and the details used in the analysis of the other 1993 data are not given. Therefore, we applied the above conditions only to the 1993 August data, but did not find any significant  $alpha$  peak around  $0^{\circ}$ .

Subsequent examination of old internal collaboration documents revealed the following facts about the 1993 August analysis.

1. Only seven of the nine ON-source runs taken in 1993 August were used in the analysis.
2. Calibrated positions of the tracking center (Section 4.1) were not used since the calibration method had not yet been established at that time. Instead, the position of the tracking center was fixed in the camera at the position of  $(x, y) = (0^{\circ}1, -0^{\circ}125)$ , which is offset from the calibrated tracking centers by  $0^{\circ}13$  on average.
3. In the image cleaning, the threshold for ADC values was fixed at 5 ADC counts.
4. Noise cut levels different from those in the standard analysis were used:  $100 \leq size < 5000$ ,  $N_{hit} \geq 4$ , and  $b \leq 0.7$ . Also, the effect of the ADC offset noise (see Section 4.2) was not corrected.
5. Another noise rejection called the “region cut” was applied. Events with centroids located within the areas of “noisy” box units were rejected in this cut. The “noisy” boxes were determined run by run and the gross number of the “noisy” boxes was eight in 1993 August.
6. The gamma-ray selection criteria were defined as follows:

$$\begin{aligned} 0^{\circ}01 &\leq width \leq 0^{\circ}25 \\ width &\leq 0^{\circ}1 + 0^{\circ}03 \frac{size}{1500} \\ 0^{\circ}1 &\leq length \leq 0^{\circ}6 \\ length &\leq 0^{\circ}2 + 0^{\circ}45 \frac{size}{1500} \\ 0^{\circ}2 &\leq dis \leq 0^{\circ}96 \\ length &\leq dis. \end{aligned}$$

The selection levels were modified slightly run by run, but no further information beyond this is available.

One can note that some of the above selection levels are different to those of Tamura et al. (1994). There seems to be some small changes in the analysis between the papers of Tamura et al. (1994) and Kifune et al. (1995).

We have applied the above conditions to the 1993 August data and the obtained  $alpha$  distributions are shown in Figure 10. Some excess of the ON-source events has

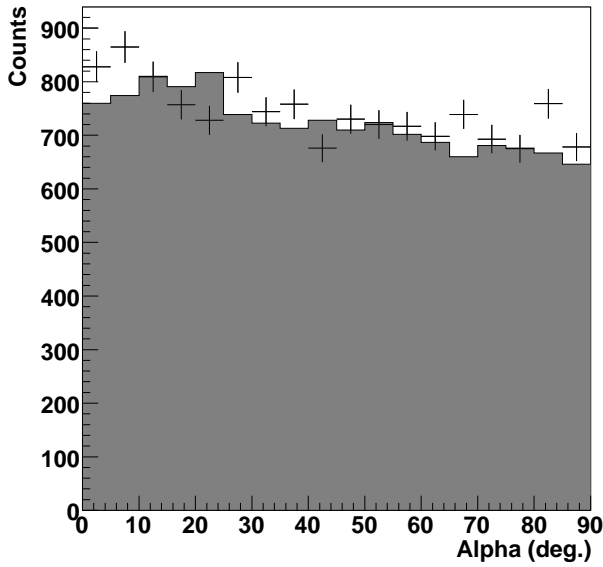


FIG. 10.— Distributions of the orientation parameter  $\alpha$  for the PSR B1706–44 data taken in 1993 August. The analysis method is based on the descriptions in the old internal documents to try to reproduce the result obtained by Kifune et al. (1995). The histogram with the error bars and the gray solid histogram are the ON- and OFF-source distributions, respectively. The number of events remaining after selections is similar to that in Figure 1 (d) of Kifune et al. (1995), although the bin sizes of the histograms differ.

been found near  $\alpha = 0^\circ$  and its statistical significance is  $2.8\sigma$  taking the events of  $\alpha$  smaller than  $10^\circ$ . However, the excess is not as sharp as the old result. Regarding the significance, Kifune et al. (1995) used a different definition, in which the background level was estimated from the ON-source events of  $\alpha > 30^\circ$  since their  $\alpha$  distributions appeared to be flat. Following this definition, the significance is enhanced by a factor of  $\sqrt{2/(1+\alpha)} \sim 1.3$ , where  $\alpha = 1/6$  is the normalization factor. It is also found from Figure 1 of Kifune et al. (1995) that the amount of the 1993 August data used in our reanalysis is roughly 1/5 of the data used in the old analysis. If we simply scale the total significance using the above factors, it turns out to be  $2.8\sigma \times 1.3 \times \sqrt{5} \sim 8\sigma$ , which is not so different from the original claim of  $12\sigma$  despite the very rough estimation. However, we think that this excess is not due to gamma rays from PSR B1706–44 since the tracking center ( $0^\circ 1, -0^\circ 125$ ) in the camera is not very close to the calibrated tracking centers and the Cherenkov images have been left affected by the ADC offset noise. Only a broad  $\alpha$  peak smeared by the source offsets and the ADC noise would be expected if it were really due to gamma rays.

A possible reason for the apparently significant gamma-ray-like signal in the previous analysis is that an initial excess has been enhanced by the complicated selection levels, and/or their run-by-run modifications but the consequent statistical penalty for the number of degrees of freedom used has been neglected. For example, the “region cut” was introduced in the name of noise rejection but the “noisy” boxes were not selected independently of the gamma-ray-like signal. If the  $8 \times 0.4 \sim 3$  “noisy” boxes are randomly selected among the total

number of boxes, 28 boxes per camera  $\times$  7 runs  $\times$  0.4  $\sim 78$ , the number of possible combinations in the “region cut” is  $\binom{78}{3} = 76,076$ , where the factor 0.4 is the ratio of the effective camera area after the  $dis$  selection of  $dis \leq 0.96$ . The total gamma-ray-like signal (number of gamma-ray-like excess events)  $z$  of a combination is represented as

$$z = \sum_{i=1}^{78} x_i - \sum_{j=1}^3 y_j, \quad (8)$$

where  $x_i \in X = \{x_1, x_2, \dots, x_{78}\}$  is the signal of the  $i$ th box (number of excess events of which the centroids are located within the box area) and  $y_j \in X$  is also a signal of a box but the index is renumbered for rejected boxes. Assuming that  $x_i$  is normally distributed with mean 0 and standard deviation  $\sigma$ , any  $z$  is also normally distributed with mean 0 and standard deviation  $\sigma' = \sigma\sqrt{78-3} = \sqrt{75}\sigma$ . However, if the maximum  $z$  is chosen among all combinations,  $z_{\max}$  is no longer distributed around 0, and in this case, the distribution has a positive offset of about  $1\sigma'$ . These kinds of offsets are accumulated by the number of degrees of freedom, and the signal can be made apparently significant just from the background fluctuations. Therefore, we suspect that the very complicated conditions in the old PSR B1706–44 analysis described above could supply sufficient degrees of freedom to generate the reported signal.

We have also investigated how much the significance can be enhanced in the real data by varying the region cut. The selection criteria used in the old analysis have been adopted except the region cut, and the number of rejected boxes in varied region cuts has been fixed at 8. In the real application, the above approximation using the factor 0.4 is not possible because the region cut is discrete, and the total number of boxes increases to 147, which is derived from 21 boxes per camera fully or partially contained in the  $dis$  selection area, multiplied by the 7 runs. The  $dis$  selection is the same in both, but they differ in how to count boxes partially contained in the  $dis$  selection area. The number of boxes per camera before region cuts is  $28 \times 0.4 = 11.2$  in the toy model, and 4 (fully contained) + 17 (partially contained) = 21 in the real application. A total of  $10^6$  combinations has randomly been sampled from the all  $\binom{147}{8} \sim 4.5 \times 10^{12}$  combinations and their significances have been calculated after applying the corresponding region cuts. They are normally distributed around a mean significance of  $2.4\sigma$  with a root mean square of  $0.24\sigma$ . The maximum significance is  $3.5\sigma$  with this number of samples. The significance obtained without using the region cut is  $2.5\sigma$  and thus the increase of the significance with the region cut actually used in the old analysis is  $0.3\sigma$  of the total  $2.8\sigma$ , which is in fact a positive enhancement, although smaller than the possible maximum offset estimated above. However, the probability of obtaining a significance greater than  $2.8\sigma$  with any region cut of 8 boxes is 6.4%, which is small to be interpreted by chance.

## 6.2. Reproducibility of the Old SN 1006 Results

Details of the old SN 1006 analysis are not given in full in Tanimori et al. (1998), and so we have followed the analysis method described by Kamei (1998) instead. The gamma-ray selection criteria were as follows:

1. for the 1996 April data,

$$\begin{aligned} 0^{\circ}04 &\leq width \leq 0^{\circ}17 \\ 0^{\circ}10 &\leq length \leq 0^{\circ}48 \\ 0.64 &\leq conc \\ 0^{\circ}1 &\leq dis \\ length &\leq dis \\ alpha &\leq 15^{\circ}, \end{aligned}$$

2. for the 1996 June data,

$$\begin{aligned} 0^{\circ}04 &\leq width \leq 0^{\circ}17 \\ 0^{\circ}10 &\leq length \leq 0^{\circ}38 \\ 0^{\circ}4 &\leq dis \leq 1^{\circ}2 \\ 3.3length - 1^{\circ}0 &\leq dis \\ alpha &\leq 15^{\circ}, \end{aligned}$$

3. for the 1997 data and events of  $size \leq 2000$ ,

$$\begin{aligned} 0^{\circ}04 &\leq width \leq 0^{\circ}13 \\ -0^{\circ}23 + 0^{\circ}13 \log size &\leq length \leq 0^{\circ}07 + 0^{\circ}084 \log size \\ 0.23 \log size &\leq conc \leq 0.42 + 0.14 \log size \\ 0^{\circ}5 &\leq dis \leq 1^{\circ}1 \\ length &\leq dis \\ alpha &\leq 15^{\circ}, \end{aligned}$$

4. for the 1997 data and events of  $size > 2000$ ,

$$\begin{aligned} 0^{\circ}04 &\leq width \leq 0^{\circ}13 \\ 0^{\circ}2 &\leq length \leq 0^{\circ}07 + 0^{\circ}084 \log size \\ 0.72 &\leq conc \leq 0.42 + 0.14 \log size \\ 0^{\circ}5 &\leq dis \leq 1^{\circ}1 \\ length &\leq dis \\ alpha &\leq 15^{\circ}, \end{aligned}$$

where the definition of *conc* is different from that originally used by Weekes et al. (1989) and is the fraction of the light detected by the camera that is contained in the brightest half of the triggered pixels. The other conditions different from the standard analysis described in Section 4 are listed below.

1. The ON- and OFF-source data were not matched in terms of the geometrical coordinates (azimuth and elevation). More data of the longer observation times listed in Table 1 without brackets were used. The background levels of the ON-source *alpha* distributions were estimated from the OFF-source distributions normalized by the observation times or from the extrapolation of the ON-source distributions of  $alpha > 30^{\circ}$ .
2. In the image cleaning, the threshold for ADC values was fixed to be 15 ADC counts.
3. The box noise cut was not used. Box noise events were manually removed looking at image centroid and shower rate distributions instead, but no details of rejected areas or periods remain. The ADC offset correction was not done. The definition of the camera edge cut was different and not based on the image distance from the camera center. Instead, images for which the centroid was located in the area of the outermost pixels were rejected.
4. The discharge noise cut introduced in Section 5.2 was not used in the old analysis but instead events

with centroids located in the bottom quarter of the camera were removed since most of the noisy pixels were located there. This cut was applied only to the 1996 data.

5. The scaler cut to eliminate the bright star effect was more complicated than described in Section 5.2. The mean and standard deviation of scaler values with no bright star in the field of the pixel were first calculated for each pixel and each run. Then signals with scaler values greater than  $8\sigma$  over the mean value were rejected from the images when the distances of the pixel from bright stars were smaller than  $0^{\circ}3$ .

In the case of the old SN 1006 analysis, calibrated positions of the tracking center had been used and therefore the accuracy of the object position was better than in the case of the old PSR B1706–44 analysis.

The above analysis procedure has been applied to the 1996 data, but the box noise cut has been used instead of the manual rejection of the noise that is impossible to reproduce. The obtained *alpha* distributions with respect to the NE rim are shown at the top of Figure 11, where the distribution of OFF-source has been normalized to that of ON-source using the observation time. A broad excess of the ON-source events is found near  $alpha = 0^{\circ}$  with the statistical significance of  $3.6\sigma$  below  $alpha = 15^{\circ}$ . The significance increases to  $4.7\sigma$  with the different assumption of the background level used by Tanimori et al. (1998), in which the background level was estimated from the “flat” region of the *alpha* plot ( $alpha > 30^{\circ}$ ) of the ON-source data. This result is similar to the old result obtained by Tanimori et al. (1998) in terms of the remaining number of events, the statistical significance level, and the *alpha* peak broadness. The middle of Figure 11 is the *alpha* distributions of the same data obtained with the same method except for the  $8\sigma$  scaler cut. The remarkable excess around  $alpha = 15^{\circ}$  in this figure has however disappeared further applying the discharge noise cut described in Section 5.2 as shown in the bottom of Figure 11. The  $8\sigma$  scaler cut was originally introduced to reduce the effect of the bright stars in the field of view, but also has the effect of reducing the discharge noise since noisy pixels also have larger scaler values. Therefore, it is possible that the excess of the top figure consists of discharge noise events remaining after the  $8\sigma$  scaler cut, which is moderately loose for discharge noise.

The above old analysis method has also been applied to the 1997 data, and Figure 12 shows the *alpha* distributions obtained. In contrast to the 1996 result, this 1997 result is quite different from the old result. No gamma-ray-like excess has been found this time and the overall features of the old result have not been reproduced. The number of remaining background events are about two times more than that of the old 1997 *alpha* plot, and therefore some additional selection criteria must have been used in the old analysis. However, no further information about the old analysis is available.

### 6.3. Vela

It is notable that all of the significances estimated in this paper have decreased from those previously reported. There are two possible reasons for this: the

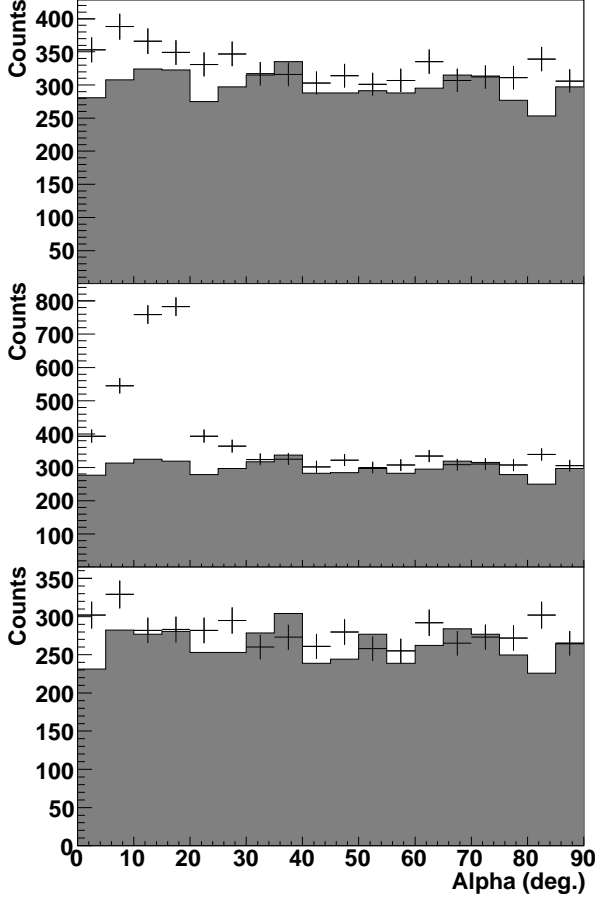


FIG. 11.— Distributions of the orientation parameter  $\alpha$  for the SN 1006 data taken in 1996 obtained using the old analysis method. The  $\alpha$  values have been calculated with respect to the NE rim of the SNR. The ON- and OFF-source distributions are represented by the histograms with the error bars and the gray solid histograms, respectively. Top: distributions obtained using the old analysis method described by Kamei (1998), middle: distributions obtained using the same method but without the  $8\sigma$  scaler cut, bottom: distributions obtained applying the discharge noise cut to the middle distributions.

previous signal for the Vela pulsar region had also been enhanced with trials in the parameter domain and/or gamma-ray events have been overcut in the present analysis since the gamma-ray selection criteria used this time are possibly too tight owing to the unmodeled effects in the simulations (see the Appendix A for more discussion). The signal from the CANGAROO-I position near the Vela pulsar obtained using the 1997 data is enhanced from  $2.5\sigma$  with the standard analysis in this paper to  $\sim 4\sigma$  previously reported by Yoshikoshi (1998), if the *size* and *length* selection levels are looser than their standard values (*size*  $\geq 180$  ADC counts and *length*  $\leq 0^\circ.45$  were used by Yoshikoshi (1998)) and more data before matching ON- and OFF-source observations (listed without brackets in Table 1) are used. We have had no standard candle in the southern hemisphere strong enough compared to the sensitivity of the 3.8m telescope and cannot fine-tune our simulation code using a real gamma-ray signal. It is consequently difficult to distinguish between these two reasons. However, in the case of the Vela 1997 data,  $2.5\sigma$  is thought to be a more conservative and reliable estimate than the previous value since it has been

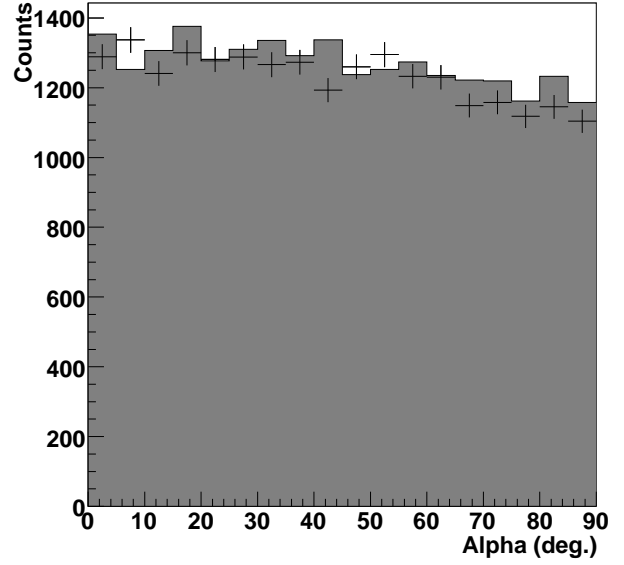


FIG. 12.— Distributions of the orientation parameter  $\alpha$  for the SN 1006 data taken in 1997 obtained using the old analysis method. The  $\alpha$  values have been calculated with respect to the NE rim of the SNR. The ON- and OFF-source distributions are represented by the histogram with the error bars and the gray solid histogram, respectively.

obtained with a common analysis method and by reducing unaccounted for degrees of freedom. The optimum level of the *length* selection is sensitive to the source location in the camera as seen in Figure 2, and thus the *length* selection level of  $0^\circ.45$  used by Yoshikoshi (1998) was conservatively selected considering the search area of the  $2^\circ \times 2^\circ$  field of view. However, the *length* selection level of  $0^\circ.45$  is very different from the optimized level of  $\sim 0^\circ.3$  for the CANGAROO-I position, and too loose to justify the above signal enhancement if we assume our simulations to be acceptable for the optimizations of the selection levels.

Dazeley et al. (2001) adopted a similar analysis method in which they have optimized the parameter selection criteria so as to maximize the quality factor using their simulations. However, they have obtained a null result applying their method to the Vela 1997 data. This difference is probably due to the different input conditions in their simulations which are described in the Appendix A in detail. Dazeley et al. (2001) have estimated the  $3\sigma$  upper limit to the integral flux from the Vela pulsar region to be  $2.5 \times 10^{-12}$  photons  $\text{cm}^{-2} \text{s}^{-1}$  above 2.7 TeV, which is about a factor of two smaller than the integral flux from HESS J0835–455 obtained by H.E.S.S. above the same threshold energy. However, their upper limit is not inconsistent with the H.E.S.S. result since only part of the emission region of HESS J0835–455 was included in their estimation as in the case of the CANGAROO-I result.

To investigate the above consistency more quantitatively, we have compared the integral fluxes between CANGAROO-I and H.E.S.S., changing the integration region around the CANGAROO-I position. Figure 13 shows the integral fluxes from the Vela pulsar region as a function of the radius of the integration region.

The circular integration regions have been centered on the CANGAROO-I position and limited to the inside of the H.E.S.S. integration region shown in Figure 8. The CANGAROO-I fluxes have been calculated considering the acceptance distribution in the field of view. The source distribution has been assumed to be uniform in estimating the average acceptance in the integration region, and as shown in Section 5.3, the fluxes are reduced by about 10% if a Gaussian source distribution is used instead. The H.E.S.S. fluxes have simply been obtained using the following formula:

$$F_r(> E_{\text{th}}) = \frac{N_r}{N} F(> E_{\text{th}}), \quad (9)$$

where  $F(> E_{\text{th}})$  and  $N$  are the integral flux and excess counts for HESS J0835–455, respectively, and  $F_r(> E_{\text{th}})$  and  $N_r$  are those integrated only inside a radius  $r$  from the CANGAROO-I position. One can note that the CANGAROO-I fluxes exceed the H.E.S.S. fluxes in the proximity of the CANGAROO-I position (the most significant excess of  $3.0\sigma$  is found at the radius of  $0^\circ 2$  from the 1993–1995 data) but the fluxes are statistically consistent with each other at large  $r$  in the both data sets, i.e., the profile of the CANGAROO-I source is more compact than that of the H.E.S.S. source. This tendency is acceptable if the gamma-ray morphology is energy dependent, since the threshold energies of CANGAROO-I are 5–10 times higher than that of H.E.S.S. There is a known example, the pulsar wind nebula HESS J1825–137, in which the morphology is energy dependent and its higher energy emission is more compact and closer to the pulsar position (Aharonian et al. 2006c).

## 7. CONCLUSIONS

We have reanalyzed the CANGAROO-I data of PSR B1706–44, SN 1006, and Vela using a consistent analysis method, in which the gamma-ray selection criteria have been optimized using gamma-ray simulations and OFF-source data. The analysis method is the simplest using a single cut or two for each image parameter and almost free from arbitrary degrees of freedom. The previously reported signals from PSR B1706–44 and SN 1006 have not been reproduced with this analysis method using the same data, whereas the signal from the CANGAROO-I position offset by  $0^\circ 13$  to the south-east from the Vela pulsar has still been detected at the  $4.5\sigma$  level. The new upper limits to the integral fluxes from PSR B1706–44 and SN 1006 at the 95% CL are higher than the upper limits obtained by H.E.S.S. and so there is formally no inconsistency between them. The emission profile of the signal from the Vela pulsar region obtained from the CANGAROO-I data has been compared with that of H.E.S.S. considering the acceptance in the field of view of the 3.8 m telescope, which quickly

drops toward the edge of the imaging camera. The expected emission profile for CANGAROO-I obtained by reweighting the diffuse emission from HESS J0835–455 with the CANGAROO-I acceptance distribution in the field of view is similar to the observed CANGAROO-I sky map, but the latter profile seems to be more compact. This difference in shape is possibly due to the fact that the threshold energy of the CANGAROO-I observations was an order of magnitude higher than that of H.E.S.S. and the energy dependent morphology of HESS J0835–455 should be studied in more detail.

We have attempted to reproduce the previous CANGAROO-I analyses for PSR B1706–44 and SN 1006 using the documented analysis methods to investigate why the significant gamma-ray signals had been obtained. “Gamma-ray-like” excesses similar to the old results have been found with the analyses carried out for the 1993 August data of PSR B1706–44 and the 1996 data of SN 1006, although they are still less significant than the old results. The old results of the other data have not been reproduced on the basis of available information, but we can conclude the following.

1. The previous reports are inconsistent with the results obtained here and as some important calibration results such as the effect of the ADC offset noise were not considered in the former analyses, their significance must be questioned.
2. The previous analyses were unduly complicated, resulting in a large number of degrees of freedom in the background event reduction. Changing the analysis conditions depending on the data sets added to the degrees of freedom, but no reasons for the differences were clarified independently of the ON-source data. Selecting noise rejection and/or gamma-ray selection levels depending on the ON-source data itself may have resulted in the apparently significant signals.

We thank all members of the CANGAROO-I team for their efforts in building and maintaining the telescopes and helping take the data used in these analyses. We also thank Dr. Bruno Khélifi, Dr. Conor Masterson, Dr. Gavin Rowell, and the H.E.S.S. Collaboration for providing us with the sky map of HESS J0835–455, the upper limit data of PSR B1706–44 and SN 1006, and related information. Thanks to the referee for useful comments helping clarify the paper. This work has been supported by a Grant-in-Aid for Scientific Research of the Ministry for Education, Culture, Sports, Science, and Technology (Japan) and the Australian Research Council.

## APPENDIX

### A. MONTE CARLO SIMULATIONS

The Monte Carlo simulation code consists of the following three parts: a) generation of EASs, b) Cherenkov light emission from the EASs and its attenuation in the atmosphere, and c) response of the telescope system. To generate EASs, GEANT 3.21 (CERN 1993) has been used with the target atmosphere modeled by 80 homogeneous layers, in which the densities have been calculated at the average heights using the US standard atmosphere. Primary gamma rays and protons have been injected at the height 50 km a.s.l., under which the effect of the homogeneous geomagnetic field of  $57.7 \mu\text{T}$  that has been calculated for Woomera using the International Geomagnetic Reference Field (IGRF)



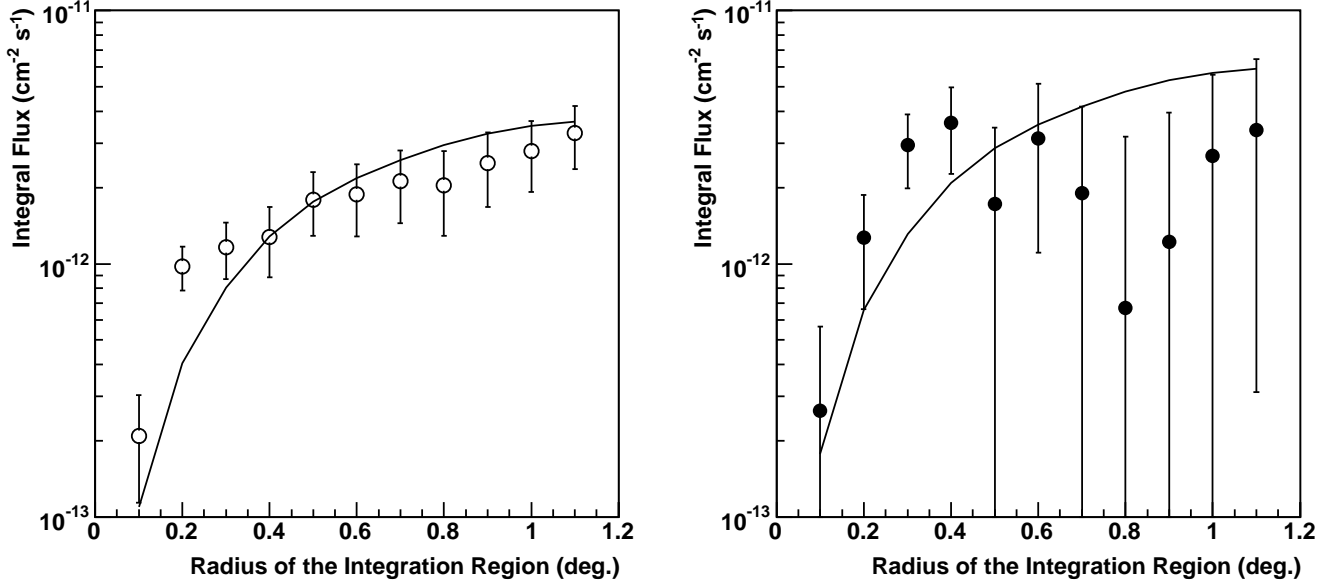


FIG. 13.— Integral gamma-ray fluxes from the Vela pulsar region as a function of the radius of the integration region. The circular integration regions have been centered on the CANGAROO-I position and limited inside of the H.E.S.S. integration region shown in Figure 8. The left and right plots are the results of the 1993–1995 data ( $E_{\text{th}} = 4.0$  TeV) and the 1997 data ( $E_{\text{th}} = 2.5$  TeV), respectively. The CANGAROO-I results are represented by the markers with the error bars, while the H.E.S.S. results are shown by the lines.

model has been incorporated. Cherenkov photons are approximately emitted from the end point of each charged particle path only if they are falling into the telescope mirror area in order to reduce the computation time. Rayleigh and Mie scatterings have been considered as the extinction of Cherenkov photons in the atmosphere. The mean free path of the Rayleigh scattering is  $2974 \text{ g cm}^{-2}$  at 400 nm, and the scale height and mean free path of the Mie scattering have been assumed to be 1.2 km and 14 km, respectively (Baltrusaitis et al. 1985). Scattered photons have been neglected, i.e., deemed to be attenuated. The computation time is further shortened by virtually reducing the number of generated photons multiplied by the following factors in advance:

$$N' = N \epsilon_t \epsilon_\phi \epsilon_r \epsilon_q, \quad (\text{A1})$$

where  $N$  and  $N'$  are the numbers of Cherenkov photons before and after the reduction, respectively, and  $\epsilon_t$ ,  $\epsilon_\phi$ ,  $\epsilon_r$ , and  $\epsilon_q$  are the atmospheric transmission factor due to the above scatterings, the fraction of the azimuthal angle range of the telescope viewed by the charged particle, the mirror reflectivity, and the quantum efficiency of the photocathode of the PMTs ( $\sim 20\%$ ), respectively.

The telescope optics has been modeled on a parabolic reflector causing the coma aberration on the focal plane plus an on-axis Gaussian blur. The blur spot size was measured using a CCD camera, with which an image of an on-axis bright star was taken and approximated to the two-dimensional Gaussian of  $\sigma = 0.04$ . Photoelectron signals due to Cherenkov radiation and incident on each PMT photocathode are integrated together with the random NSB signals and converted to a electronic waveform assuming that the signals have a common triangular pulse shape and considering their arrival time differences. Then, event triggers are examined with the conditions of the discrimination levels of three photoelectrons for each pixel and five simultaneous hit pixels. The former discrimination level has been calibrated comparing scaler values (discrimination rate per 1 ms) exposed to the NSB light with the standard NSB brightness  $2.55 \times 10^{-4} \text{ erg s}^{-1} \text{ cm}^{-2} \text{ sr}^{-1}$  (430  $\sim$  550 nm) compiled by Jelley (1958). The latter for the pixel multiplicity has been determined from lower cutoffs of  $N_{\text{hit}}$  distributions as well as its fluctuation of  $\pm 1$  pixel. One photoelectron signal corresponds to  $5.0 \pm 0.7$  ADC counts, which has been determined by equating lower cutoffs of ADC distributions with the discrimination level of three photoelectrons. This conversion factor is consistent with that calculated from parameters of the electronics. Finally, ADC and TDC values of individual pixels are calculated using the 50 ns ADC gate width and the 0.24 ns TDC resolution, and recorded in the same format as observed data.

To check the reliability of the simulations, we have tried to reproduce the trigger rate and image parameter distributions of background events. The trigger rate  $R$  can be calculated using the following formula:

$$R = A_0 \Omega_0 \epsilon \int_{E_{\text{min}}}^{E_{\text{max}}} f(E) dE, \quad (\text{A2})$$

where  $f$  is the differential cosmic ray flux, which is integrated over the simulated energy range between  $E_{\text{min}} = 500$  GeV and  $E_{\text{max}} = 100$  TeV,  $A_0 = \pi r_{\text{max}}^2 \cos \theta$  is the input area of the maximum radius  $r_{\text{max}} = 300$  m on the ground with the input zenith angle  $\theta$ ,  $\Omega_0 = 2\pi(1 - \cos \Theta_{\text{max}})$  is the input solid angle of the maximum offset angle  $\Theta_{\text{max}} = 3^\circ$  from the pointing direction, and  $\epsilon = N_{\text{triggered}}/N_{\text{input}}$  is the trigger efficiency. The cosmic ray all particle flux has been

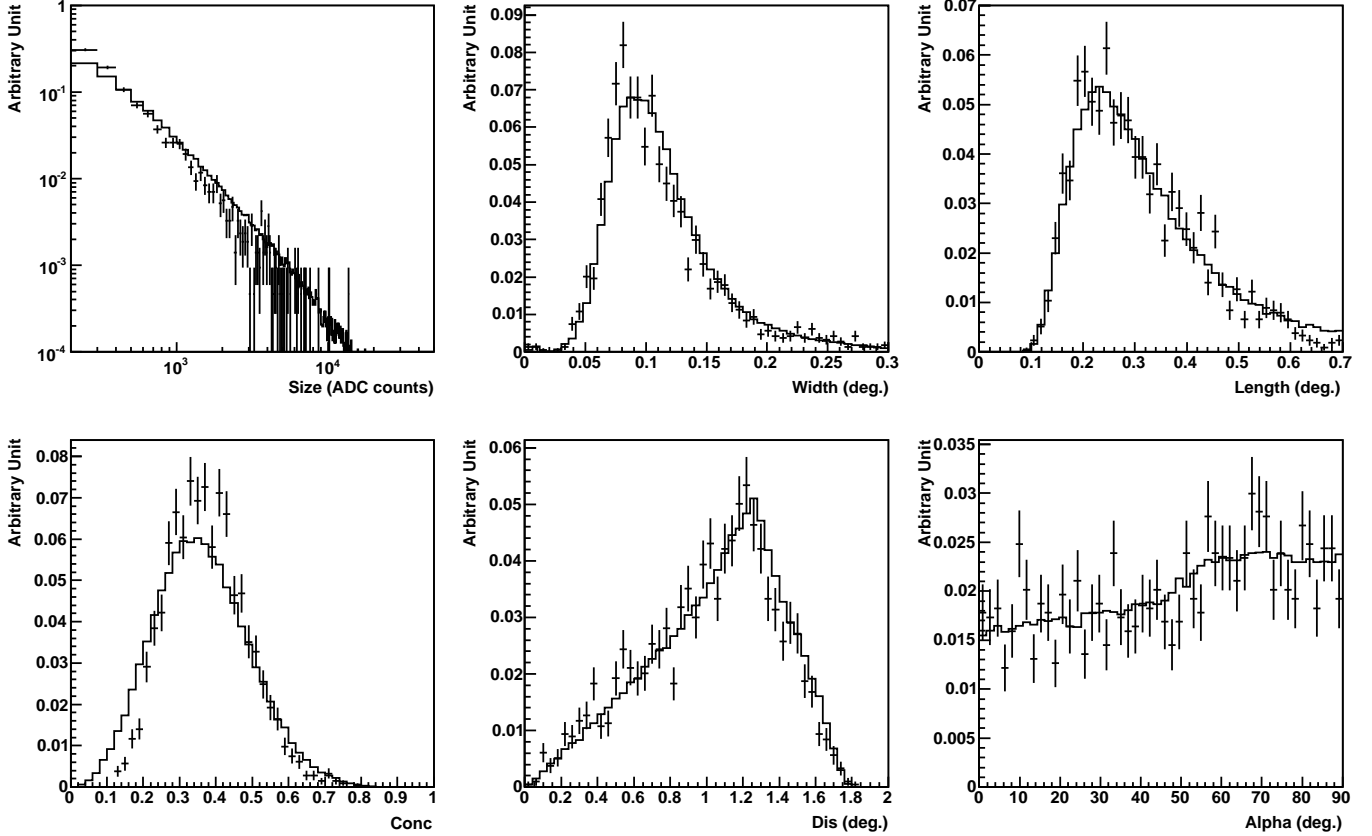


FIG. 14.— Distributions of the image parameters *size* (top left), *width* (top middle), *length* (top right), *conc* (bottom left), *dis* (bottom middle), and *alpha* (bottom right) of background hadronic events. The simulated and observed distributions are represented by the histograms with the error bars and the solid histograms, respectively. The simulated histograms have been made injecting  $10^6$  protons with the power-law energy spectrum of the index  $-2.7$ , while the observed histograms have been obtained using the OFF-source data of Vela taken in 1997. Simple noise rejections,  $b \leq 0.8$ ,  $size \geq 200$  ADC counts, and  $N_{hit} \geq 5$ , have been applied before filling the histograms, which are all normalized to 1 after filling.

obtained to be  $f(E) = 3.93 \times 10^4 (E/1 \text{ GeV})^{-2.73} \text{ m}^{-2} \text{ s}^{-1} \text{ sr}^{-1} \text{ GeV}^{-1}$  by fitting a power-law function to the direct observation data measured by Ichimura et al. (1993) between 500 GeV and 500 TeV. The input primary particles are only protons, and so it is possible that the simulated trigger rate is somewhat overestimated in comparison to the observed one. The mirror reflectivity and the average zenith angle used here are 75% and  $\theta = 15^\circ$ , respectively, to compare the result with the Vela 1997 observations. A total of 3775 events resulted in triggers out of  $10^6$  inputs and  $\epsilon = 3775/10^6 = (3.78 \pm 0.06) \times 10^{-3}$ , where the error is statistical only. Thus, the expected trigger rate is estimated to be  $4.32 \pm 0.07 \text{ Hz}$ , which is somewhat higher than the real trigger rate of 2–3 Hz. However, this result is not inconsistent with observations since the fraction of protons in the cosmic ray all particle flux is about 40% (Ichimura et al. 1993) and the trigger efficiencies for heavier particles are much smaller than that for protons (Aharonian et al. 1999). Image parameter distributions of the above simulated data are shown in Figure 14 in comparison with those of the Vela 1997 data. The observed distributions are reasonably reproduced by the simulations except for the *size* and *conc* distributions. The same tendency in *conc* has also been shown by Dazeley & Patterson (2001), and they have pointed out the possibility that the difference in *conc* is due to electronic cross-talk.

Dazeley & Patterson (2001) also tuned their simulation code by matching trigger rates and image parameter distributions between simulations and observations. However, they needed to introduce a signal loss factor to do this, which is a free parameter based on the assumption that signal intensities have been lost in the electronics. Using such a factor is inconsistent with the above-mentioned calibration results, and our simulations reproduce the observed features without it. Low-energy events and the responses to them predominantly determine trigger rates and image parameter distributions since the spectrum of primary cosmic rays has a steep power-law form and compensating for the disagreement at low energies with a single scaling factor possibly results in distortion at higher energies instead. Note that the cosmic ray spectrum can be reproduced at relatively high energies using CANGAROO-I data without the loss factor as shown by Yoshikoshi (1999). The differences between our simulations and those of Dazeley & Patterson (2001) are summarized in Table 5. A major difference other than the signal loss factor is the on-axis blur spot size of  $0^\circ 07$ , which was determined using another CCD measurement. Their larger spot size is possibly due to saturation of the CCD, but it is no longer possible to confirm this. Both spot sizes have reproduced shape parameter distributions of observed background events reasonably, but they make a significant difference in the narrower *width* distributions of simulated gamma-ray events which are displaced by about  $0^\circ 02$ . This is probably the main reason for the differences

TABLE 5  
COMPARISON OF SIMULATION DETAILS BETWEEN THIS WORK AND DAZELEY & PATTERSON  
(2001).

Input Condition	This Work	Dazeley & Patterson (2001)
EAS generation code	GEANT 3.21	MOCCA 92
Composition	p 100%	p 58%, He 32%, N 10%
Power-law index of the integral energy spectrum	-1.7	-1.65
Zenith angle at the injection point	15°	25°
Mirror reflectivity	75%	66%
On-axis blur spot size <sup>a</sup>	0°04	0°07
NSB rate <sup>b</sup>	10 MHz/PMT	8.6 MHz/PMT
Signal loss	0%	35%

<sup>a</sup> Standard deviation of the two-dimensional Gaussian. <sup>b</sup> Rate of photoelectron detections with the recoated mirror.

of the optimized gamma-ray selection criteria based on the simulations between this work and Dazeley & Patterson (2001).

#### REFERENCES

- Aharonian, F. et al. 1999, *Phys. Rev. D*, 59, 092003  
 Aharonian, F. et al. 2005a, *A&A*, 432, L9  
 Aharonian, F. et al. 2005b, *A&A*, 437, L35  
 Aharonian, F. et al. 2006a, *A&A*, 448, L43  
 Aharonian, F. et al. 2006b, *A&A*, 457, 899  
 Aharonian, F. et al. 2006c, *A&A*, 460, 365  
 Baltrusaitis, R. M. et al. 1985, *Nucl. Instrum. Methods Phys. Res. A*, 240, 410  
 Cawley, M. F. 1993, in *Proc. Towards a Major Atmospheric Cherenkov Detector II*, ed. R. C. Lamb (Calgary), 172  
 CERN. 1993, *GEANT—Detector Description and Simulation Tool*, CERN Program Library Long Writeup W5013 (Geneva: CERN)  
 Chadwick, P. M. et al. 1998, *Astropart. Phys.*, 9, 131  
 Dazeley, S. A. & Patterson, J. R. 2001, *Astropart. Phys.*, 15, 305  
 Dazeley, S. A., Patterson, J. R., Rowell, G. P., & Edwards, P. G. 2001, *Astropart. Phys.*, 15, 313  
 Dodson, R., Legge, D., Reynolds, J. E., & McCulloch, P. M. 2003, *ApJ*, 596, 1137  
 Dowden, S., Patterson, J. R., & Wild, N. 1997, *Meas. Sci. Technol.*, 8, 1258  
 Fruin, J. H. & Jelley, J. V. 1968, *Can. J. Phys.*, 46, S1118  
 Hara, S. et al. 2001, in *Proc. 27th Int. Cosmic Ray Conf. (Hamburg)*, 6, 2455  
 Hara, T. et al. 1993, *Nucl. Instrum. Methods Phys. Res. A*, 332, 300  
 Helfand, D. J., Gotthelf, E. V., & Halpern, J. P. 2001, *ApJ*, 556, 380  
 Hillas, A. M. 1985, in *Proc. 19th Int. Cosmic Ray Conf. (La Jolla)*, 3, 445  
 Ichimura, M. et al. 1993, *Phys. Rev. D*, 48, 1949  
 Jelley, J. V. 1958, *Čerenkov Radiation and Its Applications* (London: Pergamon)  
 Kamei, S. 1998, Master's thesis, Tokyo Inst. Technol. (in Japanese)  
 Kifune, T. et al. 1995, *ApJ*, 438, L91  
 Kubo, H. et al. 2004, *New Astron. Rev.*, 48, 323  
 Kushida, J., Tanimori, T., & Kubo, H. 2003, in *Proc. 28th Int. Cosmic Ray Conf. (Tsukuba)*, 4, 2493  
 Kushida, J. et al. 2001, in *Proc. 27th Int. Cosmic Ray Conf. (Hamburg)*, 6, 2424  
 Li, T. & Ma, Y. 1983, *ApJ*, 272, 317  
 Manchester, R. N., Hobbs, G. B., Teoh, A., & Hobbs, M. 2005, *AJ*, 129, 1993  
 Markwardt, C. B., & Ögelman, H. 1995, *Nature*, 375, 40  
 Muraishi, H. et al. 2000, *A&A*, 354, L57  
 Naumann-Godó, M., Beilicke, M., Hauser, D., Lemoine-Goumard, M., & de Nauroisf, M. 2008, in *Proc. 4th Heidelberg Int. Symp. on High Energy Gamma-Ray Astronomy*, ed. F. A. Aharonian, W. Hofmann, & F. Rieger (Heidelberg: AIP), 304  
 Pavlov, G. G., Teter, M. A., Kargaltsev, O., & Sanwal, D. 2003, *ApJ*, 591, 1157  
 Protheroe, R. J. 1984, *Astron. Express*, 1, 33  
 Punch, M. 1993, Ph.D. thesis, National Univ. Ireland  
 Punch, M. et al. 1991, in *Proc. 22nd Int. Cosmic Ray Conf. (Dublin)*, 1, 464  
 Reynolds, P. T. et al. 1993, *ApJ*, 404, 206  
 Rowell, G. P., Dazeley, S. A., Edwards, P. G., Patterson, J. R., & Thornton, G. J. 1998, *A&A*, 332, 194  
 Sako, T. et al. 2000, *ApJ*, 537, 422  
 Tamura, T. et al. 1994, in *Proc. Towards a Major Atmospheric Cherenkov Detector III*, ed. T. Kifune (Tokyo: Universal Academy Press), 179  
 Tanimori, T. et al. 1998, *ApJ*, 497, L25  
 Tanimori, T. et al. 1999, in *Proc. 26th Int. Cosmic Ray Conf. (Salt Lake City)*, 5, 203  
 Tanimori, T. et al. 2001, in *Proc. 27th Int. Cosmic Ray Conf. (Hamburg)*, 6, 2465  
 Weekes, T. C., Fazio, G. G., Helmken, H. F., O'Mongain, E., & Rieke, G. H. 1972, *ApJ*, 174, 165  
 Weekes, T. C. et al. 1989, *ApJ*, 342, 379  
 Weiler, K. W. & Panagia, N. 1980, *A&A*, 90, 269  
 Yoshikoshi, T. 1996, Ph.D. thesis, Tokyo Inst. Technol.  
 Yoshikoshi, T. 1998, in *Proc. Neutron Stars and Pulsars: Thirty Years after the Discovery*, ed. N. Shibasaki, N. Kawai, S. Shibata, & T. Kifune (Tokyo: Universal Academy Press), 479  
 Yoshikoshi, T. 1999, in *Proc. Towards a Major Atmospheric Cherenkov Detector VI*, ed. B. L. Dingus, M. H. Salamon, & D. B. Kieda (Snowbird: AIP), 192  
 Yoshikoshi, T. et al. 1997, *ApJ*, 487, L65